NTNU

Norwegian University of
Science and Technology

Effects of Cyclic Hypoxia in Tumor Tissue.

Ana María Acosta Roa

Medical Technology
Submission date: June 2011
Supervisor: Einar K Rofstad, IFY

Norwegian University of Science and Technology
Department of Physics

Effects of Cyclic Hypoxia in Tumor Tissue

Master Thesis

of

Ana María Acosta Roa

Institute of Physics

Norwegian University of Science and Technology, NTNU

Department of Radiation Biology

Institute of Cancer Research

The Norwegian Radium Hospital

Oslo, June 2010

Contents

Preface

This Master Thesis was developed during the spring of 2011 at the Department of Radiation Biology of the Institute for Cancer Research, at the Norwegian Radium Hospital.

Thanks to Prof. Einar K. Rofstad for the supervision, the received helpful advice from him during all the process and for giving me the chance to participate in this exciting project. I want to thank as well to my daily supervisors Dr. Philos. Jon-Vidar Gaustad and Siv. Ing. Trude Golimo Simonsen for their instruction throughout the experiments and for their valuable feedback in the writing of this Master Thesis.

I would like to thank Marit N. Leinaas too, for her technical help in the implantation of the window chambers, and to the rest of the members of the Group of Radiation Biology and Tumor Physiology for the including and warm work environment.

I am also thankful with my husband Martin for his help in the sketching of figures and in general for the patience and support that facilitated the development of this work. Thanks as well to my parents for their constant support.

Abstract

The presence of hypoxia in tumors has been related to poor prognosis and low overall survival. In particular, cyclic hypoxia has been related to higher metastatic potential. Hence, it is important to study the mechanisms involved in the response of tumors when these experience cyclic hypoxia. In this work A-07-GFP human melanoma xenografts with dorsal window chambers were used as a model to study the effects of exposure to cyclic hypoxia on tumor growth and on the morphology and function of the tumor vascular networks. First-pass imaging of a fluorescent tracer was used to study the function of tumor vasculature, and tumor vascular morphology was assessed by producing vascular masks from high-resolution images. Vascular morphology was described by quantification of vascular length density, vascular area fraction, interstitial distance and vessel diameter. The function of the tumor vasculature was assessed by quantification of the blood supply times (BSTs). It was found that exposure to cyclic hypoxia resulted in higher vascular densities, a trend towards higher BST values and decreased growth rate in the tumors. The results could be associated with enhanced angiogenesis in the tumors that received the cyclic hypoxia treatment due to overexpression of pro-angiogenic genes regulated by HIF-1α.

Chapter 1

Introduction

Tumor tissue is characterized by vascular networks with an abnormal structure that results in an increased geometrical resistance to blood flow. This enhanced resistance has consequences for the functionality of the vascular network, such as a low and heterogeneous blood supply. Hypoxic regions, *i.e.* poorly oxygenated areas, arise in tumors from the heterogeneities in blood flow and influence the tumor aggressiveness due to the activation of cellular mechanisms in order to adapt to the hostile microenvironment.

Clinical studies have shown that hypoxia is associated with bad prognosis and poor overall survival [1, 2]. Correlation between hypoxia in tumors and metastasis has been reported for different tumor lines in experimental studies [3, 4, 5, 6] showing that hypoxia in tumors results in increased metastasis, although the mechanisms for this vary from line to line. It has also been found that the effect of radiation therapy is reduced under hypoxic conditions, and that regions with intermittent hypoxia are more radio-resistent [5]. Moreover, almost all chemotherapeutic agents are active against rapidly proliferating cells. However, the rate of proliferation in solid tumors with hypoxic regions might be slower due to the longer distances to the blood vessels [7], resulting in sparing of tumor cells in chemotherapy [8].

The aim of this work is to study the effects of hypoxia exposure on tumor vascular networks. Human melanoma xenografts growing in window chamber preparations were used as tumor models, and were studied by intravital microscopy techniques. These methods are excellent for quantification of both, the morphology and the function of vascular networks.

Chapter 2

Theory

2.1 Tumor physiology

Solid tumors are conformed by cancer and stromal cells, the extracellular matrix and the vascular network [9]. Many of the differences between tumor and normal tissue stem from abnormalities in tumor vessels [10]. Tumor vasculature consists of the previously existing vessels of the tissue in which the tumor evolves and the newer microvessels that arise through a process known as *angiogenesis*, so that the metabolic demands of neoplastic cells are supplied. Both pre-existing and new vessels develop structural abnormalities which result in functional abnormalities and changes in the tumor microenvironment.

2.1.1 Angiogenesis

In order to survive, mammalian cells need to be located within the diffusion limit of oxygen from blood vessels, *i.e.*, within 100 to 200 μm [11] from the closest vessel. Therefore, for tissue to grow above the oxygen diffusion limit, it is necessary to recruit new vessels through angiogenesis. *Normal angiogenesis* occurs during fetal and post natal development as well as in wound healing, and it is a highly regulated process which takes place during brief periods and is inhibited afterwards. On the other hand, *pathological angiogenesis* is an unregulated and persistent process, characteristic of tumors and some other diseases, such as arthritis, diabetes and ocular neovascularization [12].

Likewise, tumor growth is dependent on the stimulation of angiogenesis (Fig. 2.1) achieved by disrupting the balance between pro- and anti-angiogenic factors. This is commonly known as *the angiogenic switch.*

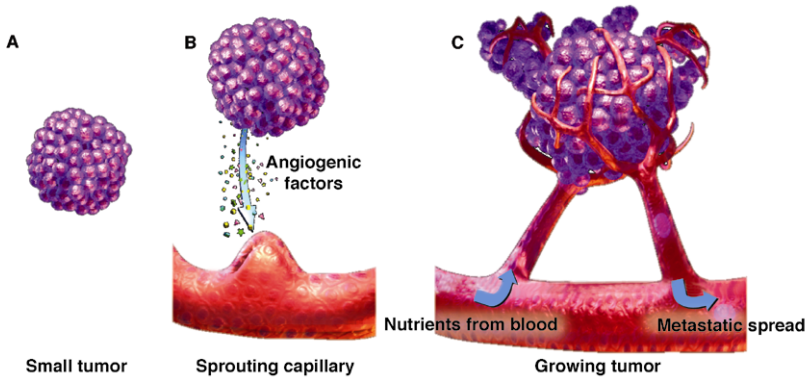

Figure 2.1: Angiogenesis is stimulated by the secretion of angiogenic factors from tumor cells which is a determining step in the survival, growth and spread of a tumor. Figure taken from reference [13].

The angiogenic switch

On a molecular level, angiogenesis is regulated by the balance of angiogenic activators and inhibitors. This balance, illustrated in Figure 2.2, determines whether an endothelial cell remains quiescent or angiogenic, thereby controlling the angiogenic switch [11, 12, 14, 15]. In solid tumors, the angiogenic switch generally activates at early stages, often at pre-neoplastic stages [15]. However, the time at which this step occur varies from one tumor to another [14].

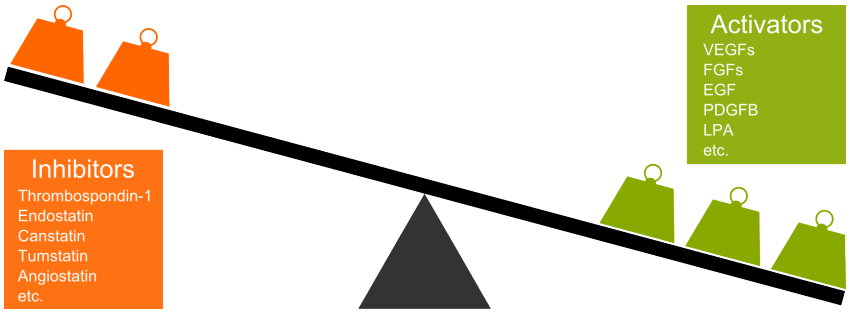

Figure 2.2: The angiogenic switch is on when the balance between pro-angiogenic and anti-angiogenic factors is disturbed towards the activators of this process.

Among the possible causes for activation of angiogenesis in tumors are: the metabolic stress to which tumor cells are subjected, *e.g.*, low pH, low O_2 and glucose concentration; mechanical stress due to pressure caused by growth of tumor mass; higher interstitial fluid pressure; inflammatory response and genetic mutations in tumors. These circumstances will lead to overexpression of angiogenic activators and/or downregulation of angiogenic inhibitors, thus, triggering the angiogenic switch [11].

Angiogenic activators

Experimental studies have revealed a number of angiogenic activators. The first angiogenic factors found were the basic fibroblast growth factor (bFGF) and acidic fibroblast growth factor (aFGF). These are proteins that can be released from cells when the angiogenic phenotype is on, and have a high affinity to heparin. Then, another protein called vascular endothelial growth factor (VEGF) was discovered as an inducer of angiogenesis as well as vascular permeability, for which, it was also called vascular permeability factor (VPF). Both, VEGF and the FGFs proteins bind to their own receptors: the VEGF receptors (VEGFR-1-3) are located specifically on endothelial cells, whereas the FGF receptors (FGFR-1-4) are also located in other kinds of cells [15].

Other important pro-angiogenic molecules are platelet-derived growth factors (PDGF) and transforming growth factor alpha (TGF-α). TGF-α activates the transformed phenotype in cells and binds to epidermal growth factor (EGF) [12]. This latter upregulates VEGF and FGF; and lisophosphatic acid (LPA), which also upregulates the VEGF levels in cells [14]. Hepatocyte growth factor (HGF) and monocyte chemoattractant protein-1(MCP-1) stimulate the growth of endothelial cells, smooth muscle cells, fibroblasts and some epithelial cells. Additionally, nitric oxide synthase (NOS) and cyclo-oxygenase-2 (COX-2) contribute in enhancing vasodilatation [11].

Angiogenic inhibitors

Angiogenic inhibitors exist naturally in cells and participate in the regulation of the angiogenic process in normal tissue. Some commonly known angiogenic inhibitors are thrombospondin-1 and -2 (TSP-1, -2). Thrombospondin is an extracellular matrix molecule that inhibits the proliferation of endothelial cells as well as their migration, growth and adhesion, and is related to the expression of tumor suppressor gene p53 [11, 15]. This tumor suppressor gene upregulates the production of thrombospondin in cells. Another angiogenic inhibitor is interferon, which acts by inhibiting migration of capillary endothelial cells [16]. Metalloproteinase inhibitors (MMPs inhibitors or TIMPs) also have an anti-angiogenetic effects cooperating in the degradation of the extracellular matrix [11]. Anti-adhesive peptides and the synthetic protease inhibitors are fabricated angiogenesis inhibitors. The first ones act by blocking the interaction of $\alpha_V\beta_3$ and $\alpha_5\beta_1$ integrins, which are angiogenesis mediators, with the extracellular matrix ligands; and the latter have shown clinically an anti-tumor and anti-metastatic effect [16]. Angiostatin and endostatin are tumor-derived inhibitors of angiogenesis. Angiostatin participates in the inhibition of angiogenesis by blocking endothelial migration and proliferation, whereas

endostatin restrains microvascular endothelial cell proliferation and survival, thereby complicating tumor growth and metastasis [11, 16].

Anti-angiogenic agents have been studied lately for their applications in cancer therapy. The fact that anti-angiogenic therapy could reduce the occurrence of metastasis and prevent tumor growth, together with the possibility of normalization of pathologic vascular networks [9] has given rise to a different approach for cancer therapy.

Sprouting and intussusceptive angiogenesis

The angiogenic process can occur either by *sprouting* of new vessels or *intussusception* of existing vessels, as illustrated in Figure 2.3.

Sprouting angiogenesis starts with the dissolution of the basement membrane of a vessel into the extracellular matrix, then, endothelial cells move towards the angiogenic stimulus and proliferate leaving a trail along their migration path where lumen develops and canalization takes place. Subsequently, branches emerge from the main trail, often conforming loops, and vessels are then covered by pericytes and a basement membrane forms in them, thereby marking the maturation of the new branches [17].

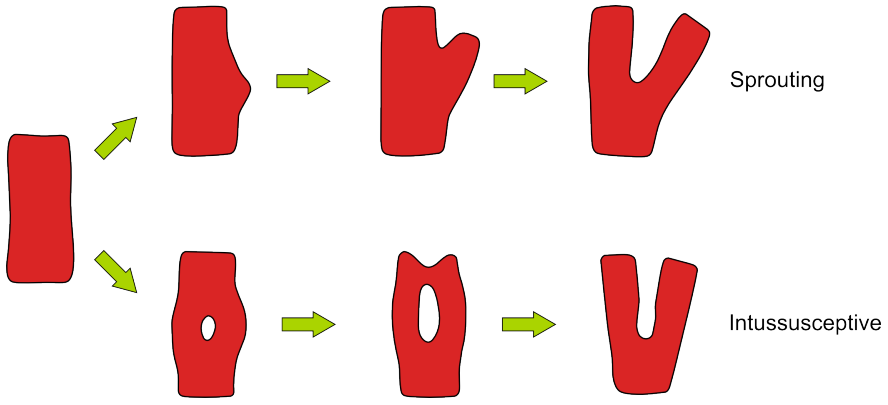

Figure 2.3: The angiogenic process can take place as sprouting of new vessel or through intussusception of extra cellular matrix columns into the blood vessels.

The other possible angiogenic mechanism is vessel splitting, better known as *intussusception*, which occurs by insertion of extracellular matrix columns transcapillary pillars. This can happen *in vivo* if endothelial cells proliferate inside vessels and thereby a lumen is formed in the vessel and grows dividing it and permitting

the insertion of transcapillary pillars. Further growth of this columns can lead to subsequent partitioning of the vascular network [17, 18].

The mechanism by which angiogenesis occur may depend on the type of tissue or organ where the process takes place due to different abundance or availability of vessels as well as endothelial cell precursors [18].

2.1.2 Tumor vasculature

The vascular network in tumors differs from that in healthy tissue by presenting abnormalities in its morphology. These structural abnormalities are responsible for alterations in the blood flow, *i.e.*, functional abnormalities. In the following subsection, a review of the morphological abnormalities is presented and its consequences will be discussed as part of the tumor blood flow section.

Morphological abnormalities of vascular networks in tumors

Structural abnormalities in the vasculature arise from the disturbed balance between angiogenic inhibitors and activators which leads to a unregulated and, thus chaotic, development in the vascularity, thereby inducing changes in the morphology, as shown in Figure 2.4.

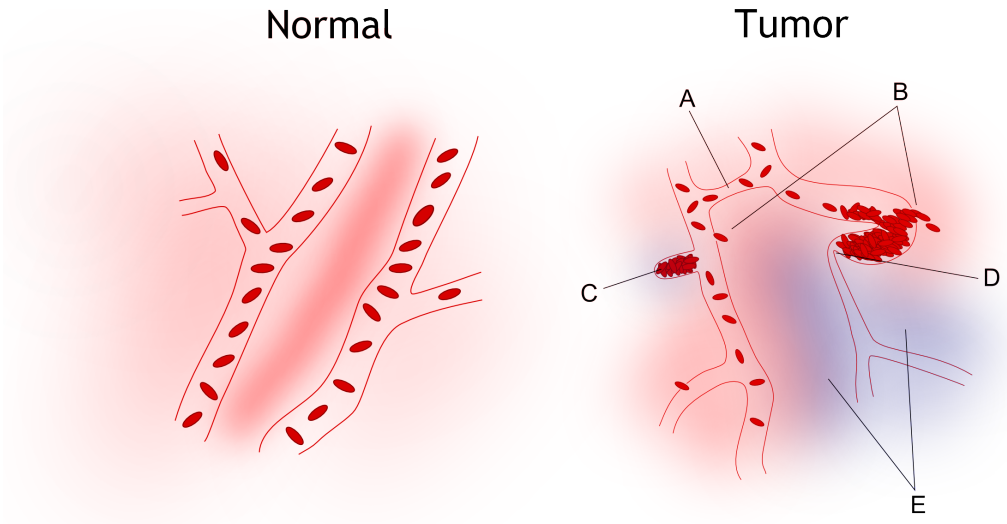

Figure 2.4: Normal vasculature (**left**) and tumor vasculature (**right**). The tumor vasculature shows multiple anormalities: **A:** arteriovenous shunts, **B:** leakage in vessels, **C:** capillaries with blind ends, **D:** vessel obstructions that can lead to thrombosis and **E:** hypoxic regions.

The possible morphological abnormalities in tumor vasculature can be divided in the following three categories [19], as listed below:

1. **Irregularities in the vessel walls:** incomplete or missing endothelial lining, interrupted or absent basement membrane, blood channels lined by tumor cell cords and lack of contractile wall components.

2. **Abnormalities in single vessels:** changes in vessel diameter, contour irregularities, tortuosity and elongation of vessels.

3. **Vascular network architectural abnormalities:** heterogeneous distribution of vessels, expansion of inter-capillary space, arteriovenous shunts and loss of hierarchy.

These irregular architectural features have serious consequences in the blood flow functionality. This will be discussed in the following section.

2.1.3 Blood flow

The blood flow rate, Q, in either normal or tumor vasculature, is directly proportional to the pressure gradient between the arterial and venous ends of the network Δp, and inversely proportional to the flow resistance, FR [20], *i.e.,*

$$Q = \frac{\Delta p}{FR}. \tag{2.1}$$

The flow resistance FR of a vascular network, is a complex function dependent of the morphological parameters of the vascular network (such as number of vessels, their branching pattern, length, diameter, etc.), and of the rheology of the blood [20], *i.e.* it will also depend on the viscosity η of the blood: the more viscous the blood, the more resistance the vessel will impose to the flow. This means that the flow resistance FR is a parameter that comprises the geometrical resistance and the viscous resistance:

$$FR = Z\eta. \tag{2.2}$$

A simplified model to describe the flow resistance in a blood vessel is given by the Hagen-Poiseuille equation [21] for a laminar flow of blood with viscosity η in a cylindrical rigid vessel of radius R and length L as,

$$FR = \frac{8\eta L}{\pi R^4}, \tag{2.3}$$

from where, the geometrical resistance that a vessel exerts on the blood flow Z is defined as,

$$Z \equiv \frac{8L}{\pi R^4}. \tag{2.4}$$

Hence, the blood flow rate in terms if the pressure gradient Δp, the blood viscosity η and the geometrical resistance Z can be mathematically expressed as [20, 21]:

$$Q = \frac{\Delta p}{\eta Z}. \tag{2.5}$$

Equation 2.5 shows the impact of the geometry of a vessel on the circulation in it. This can be extrapolated to elucidate the importance of the geometric resistance of the vascular network of a tumor as a whole on its functionality. Therefore, the conjugation of the irregularities in the morphology of tumor vascular networks and the increased viscous resistance will result in a reduced and less efficient blood flow inside the tumor.

Functional abnormalities of vascular networks in tumors

Common functional abnormalities observed in tumor vascular networks are intermittent blood flow and variations in its speed and direction, arteriovenous shunt perfusion, increased vascular fragility, blood extravasation and hemorrhages, obstruction of vessels, thrombosis, increased viscous resistance and hemoconcentration [19].

Altogether, the morphological and functional abnormalities in the vascular networks of tumors result in an irregular blood flow with temporal and spatial heterogeneities. These heterogeneities can lead to certain conditions in the microenvironment of the tumor such as increased interstitial fluid pressure, decreased pH and pO_2 gradients.

2.1.4 Hypoxia

The reduced blood perfusion in tumors and the higher metabolic rate of neoplastic cells alter the balance between oxygen supply and demand leading to spatiotemporal variations of oxygen tension in tumors [22]. Measurements of oxygen tension in normal subcutaneous tissue obtained with Eppendorf electrodes [23] show that normal tissue usually have pO_2 values ranging from approximately 30 to 70 mmHg, with no values under 10 mmHg. Yet, the oxygen tension measured in lymph node metastases of head and neck tumor was much lower, with a median value of approximately 10 mmHg, as presented in Figure 2.5.

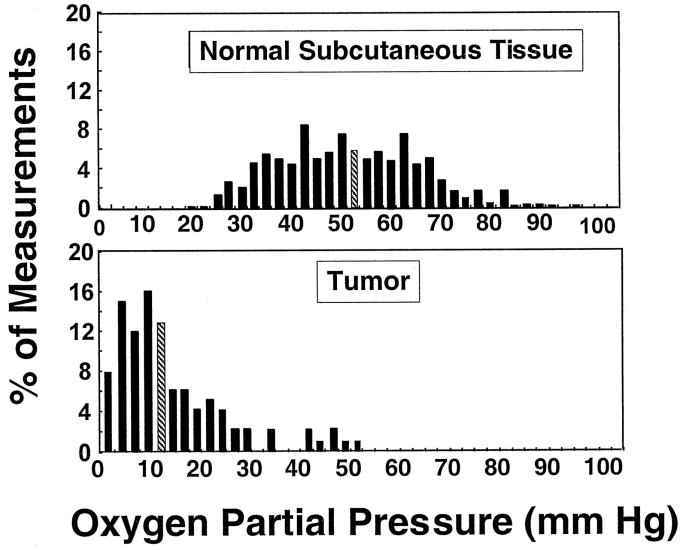

Figure 2.5: Oxygen pressure in a lymph node metastasis of a head and neck tumor and in the surrounding normal s.c. tissue measured with Eppendorf oxygen electrodes [23, 30]. The median pO_2 value is marked by the hatched bar.

Hypoxia is defined as low oxygen tension in tissue, usually referred to an oxygen tension under a threshold of $pO_2 < 10$ mmHg [24, 25, 26, 27], and can be caused by transient interruptions of blood vessels, or by limited oxygen diffusion to a certain region, yet these two mechanisms are not mutually exclusive [22]. Hypoxia is classified in two subgroups according to its origin, as:

1. **Chronic hypoxia.** Occurs due to permanent limitations in oxygen diffusion, typically arising adjacent to necrotic regions, and therefore is also termed *diffusion-limited hypoxia*.

2. **Acute hypoxia.** Due to transient limitations in tumor blood perfusion, blockage or changes in flux which is why it is also called *perfusion-limited hypoxia*. This type of hypoxia can occur cyclicly, and when so, it is termed *cyclic hypoxia*.

Hypoxia has been correlated to limited proliferation and differentiation in tumors, nevertheless, it is well known that hypoxia stimulates adaptability to a hostile microenvironment thereby increasing tumor aggressiveness [1, 2, 3, 4, 5, 6, 8, 11, 22, 24, 27]. Hence, it is of great importance to understand the pathways underlying the hypoxic mechanisms in tumors.

2.1.5 Diffusion-limited hypoxia

Thomlinson and Gray [28, 29] observed two types of cells in histological sections of bronchial carcinoma: cells that were proliferating normally, and others that were dying or already dead; and that the main reason of this cell death was the low oxygen content in the regions where these cells were found, due to the long distances between them and capillaries.

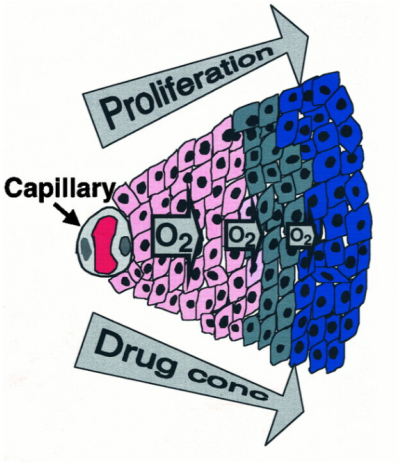

Figure 2.6: Cross-section of a capillary surrounded by tumor cells illustrating the decrease in oxygen concentration in the tissue dependent to the distance to the capillary. Normoxic cells (shown in pink) are close to the capillaries, whereas hypoxic and anoxic cells (shown in grey and blue, respectively) appear further away from the vessels, to approximately a distance of 70 μm. Figure from reference [30].

In between the region of the necrotic and normoxic[1] cells, tissue with enough oxygen and nutrients to proliferate but too little oxygen to be radiosensitive was found. This was denominated hypoxic tissue and was mainly located at approximately 70 μm from a blood vessel and can therefore be classified as *diffusion-limited* or *chronic hypoxia*.

Diffusion limited hypoxia can also arise from the geometrical resistance in the vasculature. Figure 2.6 shows a capillary cross section environed by tumor cells which decrease in oxygen concentration the further they are from the vessel: normoxic tissue is found closest to the capillary, diffusion-limited or chronic hypoxic tissue is found between anoxic tissue and the normoxic tissue. The limited diffusion of oxygen and nutrients in tumors has negative implications for drug delivery in chemotherapy in addition to ionizing radiation increased resistance, although proliferation far from the vessels can as well be restricted due to the lack of nutrients.

[1] At a normal oxygenation status.

2.1.6 Perfusion-limited hypoxia

Temporary occlusions of vessel inside tumors can be caused by compression of the microvessels due to fast division of the neoplastic cells or by agglomeration of relatively large white blood cells [31]. In addition, changes in blood flow direction also result in regions of acute or perfusion-limitted hypoxia. Changes in the oxygenation status of tumors can occur cyclicly throughout the life span of the cells, moreover, there has been evidence that some blood vessels in tumors get blocked randomly for periods of time ranging from around 60 seconds to a couple of hours [32] which has been the reason why this type of hypoxia has also been denominated *cyclic* or *intermittent hypoxia*.

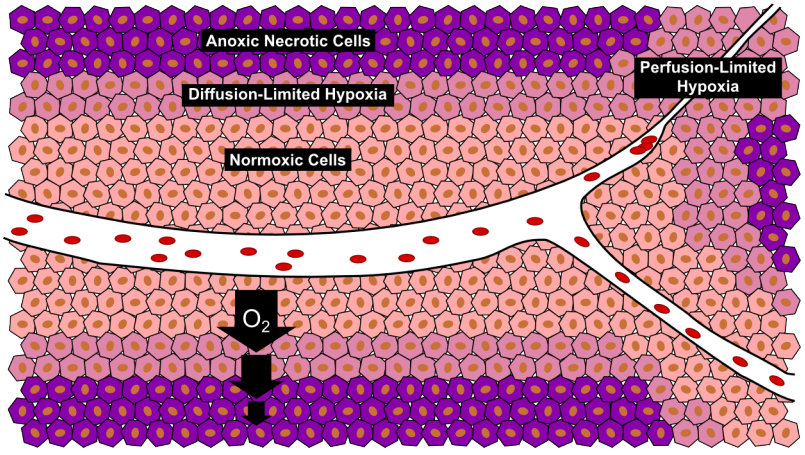

Figure 2.7: Perfusion-limited hypoxia arises from transient obstructions in the blood flow which can last from seconds to some hours and may repeat cyclicly, whereas diffusion-limited hypoxia occurs due to cell proliferation outside the oxygen diffusion range from the closest capillary. (Adapted from reference [29].)

As illustrated in Figure 2.7, acutely hypoxic regions are most likely to appear close to capillaries. The existence of acute hypoxia has been demonstrated in a number of experiments. Chaplin *et al.* injected a short diffusion range fluorophore intravenously in mice with murine squamous carcinoma, irradiated the tumors, dissected them and sorted the tumor cells by their fluorescence intensity (as an indicator to their proximity to the vessels). Afterwards, the viability of these cells was assessed using the soft agar clonogenic assay. These researchers found that there were radioresistant cells in the tumors even adjacently to blood vessels, which was most likely due to the presence of perfusion limited hypoxia [33]. This same research group reported that 20-minute-interval sequential injection of fluorescent markers in mice with the same type of tumors as in the previous experiment resulted in a mismatch of the staining in the tumors which indicated intermittent perfusion

due to transient occlusion of vessels during periods of at least 5 minutes [34]. These mismatch regions appeared randomly distributed throughout the tumors [34].

More recently, occurrence of cyclic hypoxia was demonstrated by measuring the temporal variations of oxygen tension in human melanoma xenografts with fiber optic oxygen sensitive probes continuously for one hour [25]. The presence of chronic and acute hypoxia in this same tumor line was also evidenced by differentiating the fraction of hypoxic cells with pimonidazole staining (a marker of diffusion limited hypoxia) from the radioresistant cells, which comprised the chronic and acutely hypoxic cells in these tumors [6].

The relatively short distance from the blood vessels to acutely hypoxic cells positions them on a higher energy state than the chronically hypoxic cells, thereby facilitating intravasation and spread through the circulation. Intermittent hypoxia in tumors has been related to higher metastatic occurrence, which has been reported for different tumor lines [3, 4, 5, 6] confirming that for most of the studied tumors, cyclic hypoxia treatment results in increased metastasis, although the mechanisms and incidence vary from one tumor line to another. In particular, A-07 melanoma tumors *in vivo* exposed to intermittent hypoxic stress present increased angiogenesis, perfusion and metastatic dissemination [6].

2.1.7 Consequences of hypoxia

Hypoxia induced gene expression

Poorly oxygenated tumor tissue manifest a series of changes as an adaptive response in order to survive and proliferate in the hostile microenvironment. Among the adaptation responses, occurs gene expression for a more effective supply and utilization of oxygen and nutrients. This gene expression is mostly regulated by the *hypoxia inducible factor 1* (HIF-1) [24, 35, 36, 37, 38].

HIF-1 is an heterodimer consisting of a constitutively expressed nuclear protein independent of the oxygen tension, the HIF-1β subunit, and one inducible subunit HIF-1α that is a cytoplasmic protein dependent on oxygen concentration [24, 37, 38].

As shown in Figure 2.8, under normoxic conditions HIF-1α is constantly degraded by the ubiquitin-proteasome system, whereas for hypoxic circumstances the

HIF-1α subunits are translocated to the nucleus. Subsequently, HIF-1α and HIF-1β dimerize and give rise to a HIF-1 protein that binds to target genes in the DNA, activating the transcription of the genes expressed under hypoxic conditions [24]. Some of these genes are vascular endothelial growth factor (VEGF), platelet-derived growth factor (PDGF), erythropoietin, inducible nitric oxide synthase (iNOS), epidermal growth factor (EGF), transforming growth factor-beta (TGF-β), insulin-like growth factor-2 (IGF-2), glycolytic enzymes and glucose transporters [19]. From these genes, VEGF, PDGF, erythropoietin, EGF and iNOS are pro-angiogenic factors, this results in *hypoxia-driven angiogenesis*.

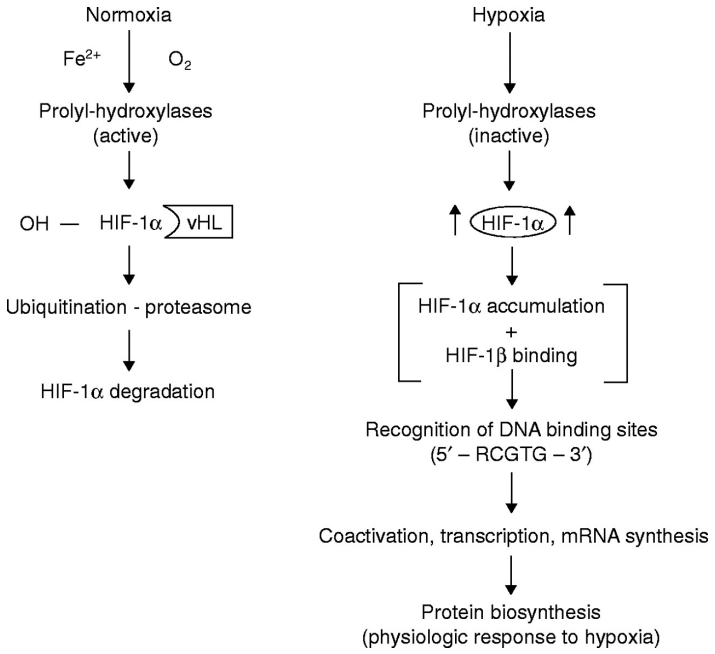

Figure 2.8: Effects of the oxygen level on HIF-1α regulation. In a normoxic environment, the ubiquitin-proteasome system degrades HIF-1α, whereas in hypoxic conditions HIF-1α heterodimerizes with HIF-1β and binds to elements in the DNA which activate transcriptions and mRNA synthesis that result in the expression of proteins mediated by hypoxia [24].

Hence, HIF-1 induces an aggressive phenotype in tumors, since a higher vascularization in tumors facilitates metastasis since cancer cells are more likely to enter the circulation and spread than in tumors with lower vascular densities [24, 39], and because angiogenesis allows the growth in tumors [11, 12]. Moreover, PDGF, EGF, IGF-2 and TGF-β are genes that stimulate tumor growth, cell proliferation and survival. In addition, the glycolytic enzymes and glucose transporters cooperate in the metabolic adaptation of hypoxic tumors promoting glucose uptake ensuring that the metabolic requirements are met [24]. These hypoxia-induced mechanisms are summarized in Figure 2.9.

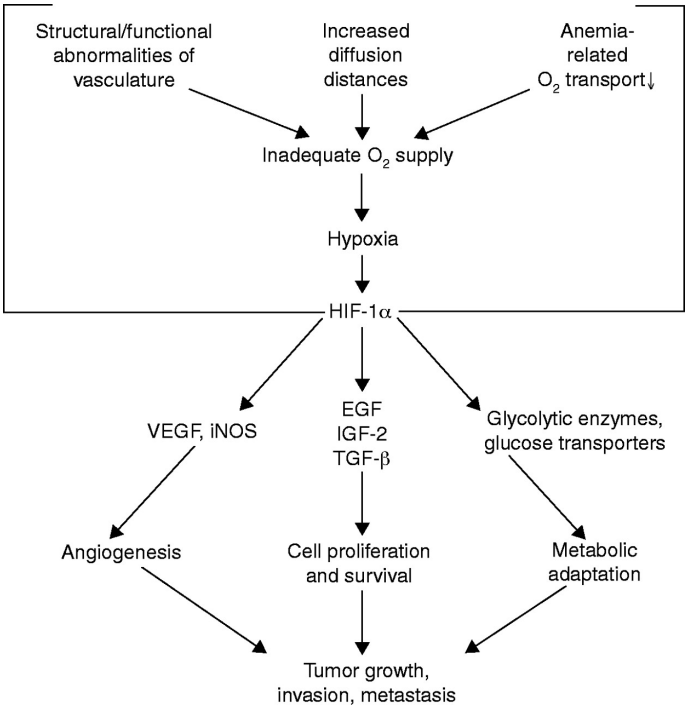

Figure 2.9: Causes and consequences of hypoxia and expression of HIF-1α in tumors. Dimerization of HIF-1α in hypoxic cells activates the transcription of genes that favor angiogenesis, cell proliferation and survival, and metabolic adaptation to the hostile environment, this responses are related to malignancy in tumors [24].

Effects of hypoxia in cancer treatment

Differences in radiation sensitivity due to the oxygen content in cells were first quantified by Gray *et al.* in their study of radiation-induced growth inhibition of a root of the *vicia faba* bean [29, 40]. This phenomenon is known as the *oxygen effect*. The oxygen effect can be quantified by the calculation of the *oxygen enhancement ratio, OER,* defined as the ratio between the doses needed to obtain the same therapeutic effect in hypoxic tissue compared with normoxic tissue [29]. In mammalian cells, this ratio ranges between 2.5 to 3 for x-ray irradiation [29, 30] which, as shown in Figure 2.10 (Left), indicates that for a given radiation dose the difference in the cell surviving fraction can vary in several orders of magnitude. However, the OER decreases with increasing the density of the ionizing radiation (large for low LET[2] radiation such as x-rays, medium for neutrons and insignificant for α-particles [29]).

[2]LET is the linear energy transfer characterizing a certain radiation defined as the average energy dE imparted locally in traversing a distance dl [29].

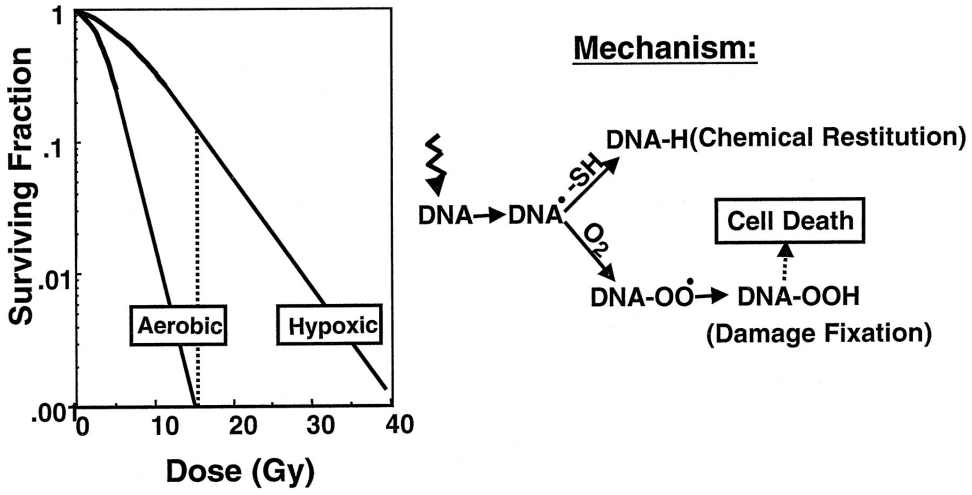

Figure 2.10: **Left:** Typical survival curves to ionizing radiation for mammalian cells under aerobic and hypoxic conditions, the dotted vertical line corresponds to a dose of 14 Gy. **Right:** DNA damage caused by ionizing radiation can be restored by interaction with a sulfhydryl group, or can be made permanent in the presence of oxygen by formation of organic peroxides. Taken from reference [30].

The absorption of ionizing radiation produces fast charged particles that interact with the biological tissue giving rise to short-life ion pairs which produce free radicals. These free radicals can break chemical bonds and damage the DNA, creating a DNA radical that might be chemically restituted if it undergoes reduction by reacting with a non-protein sulfhydryl (-SH) in the absence of oxygen. Yet, in the presence of oxygen, organic peroxides are formed, making the damage to DNA non-restorable [29, 30]. These two pathways are illustrated in Figure 2.10-Right. Hence, hypoxia is related with less radio-curability in tumors.

Regarding chemotherapy, the effects of hypoxia can be associated to the metabolism in the hypoxic cancer cells, or to the morphology of vascular network in the tumor. In the first case, the lack of oxygen, nutrients and reduced glucose in hypoxic cancer cells can cause an arrest or a slower pace in their course through the cell cycle, which results in slower proliferation of hypoxic cancer cells [30]. Since, the majority of anticancer drugs are targeting rapidly proliferating cells, slow- and non-proliferating hypoxic cancer cells might be spared [8]. In the second case, as oxygen has a diffusion limit distance from a vessel, diffusion of the anticancer drugs is limited by proximity to capillaries. This also implies that the concentration of the drugs will be higher close to vessels and might be insufficient in regions with chronic hypoxia. Poorly vascularized and necrotic regions result in a decrease in uptake of therapeutic agents. This is specially worse for larger tumors where there is a greater necrotic

volume. Transient blockages of vessels in the tumors will also prevent a sufficient distribution of anticancer drugs in acutely hypoxic tumor cells. The center of a tumor is characterized by a high interstitial pressure in comparison to the periphery leading to low drug uptake and heterogeneous drug distribution. In general, the geometrical resistance to the blood flow imposed by the vasculature will difficult an appropriate distribution of chemotherapeutic agents in tumors [30].

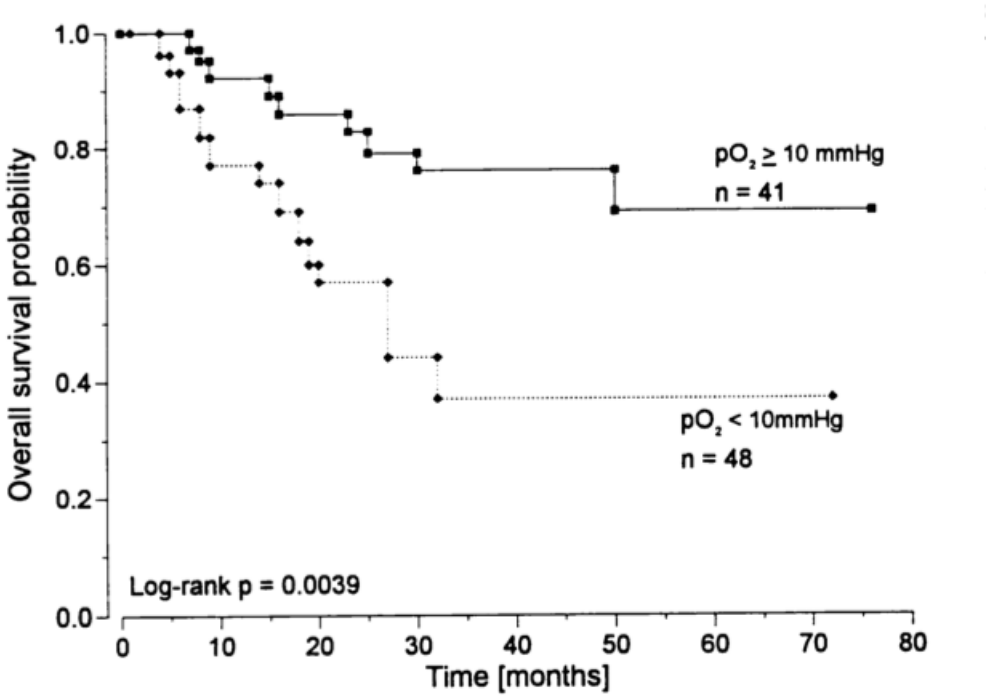

Figure 2.11: Kaplan-Meier curves showing the overall survival probability for 89 patients with cervical tumors. All the patients were treated with curative intent and divided into two groups according to tumor oxygenation status. Taken from reference [41].

Figure 2.11 shows the of overall for 89 women with cervical tumors with diameters of at least 3 cm. The tumor oxygenation status was measured with Eppendorf needles and, subsequently, patients were divided in those with normal oxygen tension tumors ($pO_2 \geq 10$ mmHg), and those with hypoxic tumors ($pO_2 \leq 10$ mmHg) [41]. All patients were treated with curative intent. From these curves, it is evident that the presence of hypoxia is related to a poor prognosis and overall survival probability.

2.2 Tumor model systems

2.2.1 Xenografts

The term *xenograft* refers to the transplantation of living cells, tissue or organs from one species to another [29]. Cells from human tumors transplanted to animals, are often used as model system for cancer in humans. The suitability of xenograft models varies among different cancer types, for example, melanomas and tumors from lungs and colon have generally resulted in greater success in xenograft studies than tumors from breasts and ovaries. Human cancer cells are normally rejected through immune reactions in animals with a normal immune system. Therefore, immunodeficient animals are commonly used for cancer research, although the possibility of rejection of cancer cells is always present.

An example of this is the BALB/c nu/nu mice. This type of mice originated from spontaneous mutation at the NIH Animal Genetic Resource [42] with lack of a thymus from birth. Thus, these mice cannot produce T-cells (being therefore immunodeficient) which makes them suitable for allografts, xenografts and malignant tissue research. In addition, these mice are hairless with albino background which can facilitate intravital microscopy techniques. The lack of thymus and hair in these mice arises from an autosomal recessive nude gene in homozygous (nu/nu). These mice are different than the heterozygous (nu/+) which have a normal thymus and can be haired [43].

A major advantage with xenografts is that the histological features of the original tumor are mostly preserved [44]. Nevertheless, the supporting tissue and the vasculature will come from the animal. Human tumor xenografts normally have a doubling-time of about a fifth of the time observed in humans. This increased growth rate is an advantage experimentally for practical reasons, but may influence the results in studies that are sensitive to tumor growth rate [29].

2.2.2 Spheroids

Certain kinds of cells are capable of growing as *spheroids*. To obtain cellular growth in spheroid manner, cells must be cultivated to prevent them from attaching to a solid surface [29]. After subsequent individual cell divisions, the cells must remain attached to each other in order to conform increasingly larger spherical structures. Cells in the spheroids depend on a passive diffusion of oxygen and nutrients from the surrounding medium. When the radius of the spheroid is beyond the diffusion limit of oxygen, the center of the spheroid will begin to have a deficiency in

oxygen combined with a accumulation of waste which can result in a central necrosis as growth continues [29]. Spheroids are good *in vitro* models of a avascular tumors. Nevertheless, not all tumor cell kinds are able of growing as spheroids.

2.3 Intravital microscopy

Intravital microscopy consists of microscopically imaging intact living tissue. Tissue preparations for intravital microscopy can be either chronic transparent windows, acute preparations (where the animal in research is prepared surgically to gain direct access to inner organs), or *in situ* preparations [46]. Transparent window chambers implanted in the dorsal skinfold of mice are commonly used models for the study of tumor vasculature with intravital microscopy. In this case, a tumor grows inside of one of the skin layers, under a glass window. This glass window makes it possible to image the vascular network of the tumor. In order to achieve good visualization of the vasculature, fluorescent contrast agents can be injected intravenously which, after a short time, distribute throughout the vascular network of the tumor.

2.3.1 Interactions between light and matter

The transit of light through a material leads to exchange processes between the light and the molecules in the material [47]. These interactions can result in changes of the direction, polarization and energy of light through different absorption and energy distribution processes. If the energy of the incoming photons is equal to or greater than the energy difference between two energy levels in a molecule, the molecule can absorb the energy and excite to a higher energy level. Both electronic, vibrational and rotational energy levels can be excited. Since the energy of the incoming photons is dependent on the wavelength of light, it is possible to use light with different wavelengths to selectively excite different molecules or different energy levels in the same molecule. After an excitation takes place, the excited molecule will expel the absorbed energy and return to the basal state. This de-excitation can occur through different processes. The most important ones are illustrated in the Jablonski diagram (Figure 2.12). From these processes, fluorescence and phosphoresce involve the emission of light. Phosphorescence comprises forbidden transitions between electronic energy levels with different spin quantum number J.

Fluorescence consists of electronic relaxation without changing the spin quantum numbers for the electrons ($\Delta J = 0$), with further emission of a photon with an energy equal to the excited energy gap. Fluorescence only occurs from the lowest excited condition to the basal state [48]. In the absence of other relaxation processes,

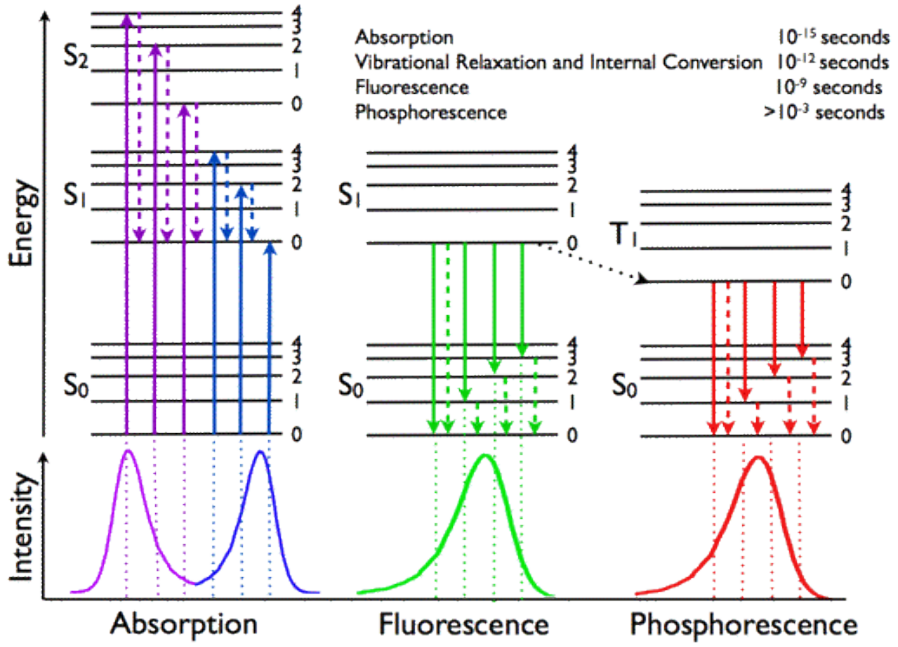

Figure 2.12: The Jablonski diagram and spectra of absorption, fluorescence and phosphorescence. Solid arrows point to radiative transitions through absorption (shown in violet and blue) or emission of a photon by fluorescence (displayed in green) or phosphorescence (marked in red). Non-radiative transitions are pointed with dashed arrows. Transition $S_{1,0} \rightarrow T_{1,0}$ (subscripts correspond to the electronic state and vibrational sublevel, respectively) is termed *intersystem crossing* since it occurs between two states of distinct spin multiplicity and is non-radiative. Under the Jablonski diagram, representations of the absorption, fluorescence and phosphorescence spectra are shown [45].

fluorescence has a life-time of about 10^{-9} to 10^{-8} seconds. Other non-radiative processes compete with fluorescence, among them, internal conversion, dissociation, chemical reactions and ionization. The emitted fluorescent light has less energy than the excitation light. The molecule releases the remaining excitation energy through non light emitting transitions between vibrational levels within the same electronic energy level. The result is that the fluorescent light gets a shift towards longer wavelengths compared to the excitation light. This is called *Stokes shift* and makes it possible to separate excitation light from fluorescence light with the help of optical filters.

2.3.2 Fluorescent markers and contrast agents

The ability of molecules to absorb and emit light with certain frequencies can be exploited to detect special molecules in a test volume based on the emission spectrum. Molecules can be naturally fluorescent (a phenomenon called *autofluorescence*) or can fluoresce due to the presence of other fluorescent molecules.

Endogenous fluorophores are autofluorescent contrast agents that occur naturally in a sample. Several molecules that occur naturally in cells are auto-fluorescent, such as NADH, flavins, elastin and collagen [47]. This property can be utilized to image special structures inside the cell in addition to different cellular processes.

Exogenous fluorophores are fluorescent molecules that can be attached specifically to biological structures. There exist a variety of these fluorophores which vary in specificity, sensitivity and emission spectra. Some basic requirements for an exogenous flurophore are solubility, specificity for association with targets, high quantum emission efficiency, stability and low probability of photobleaching[3]. When using different fluorophores simultaneously, it is important that the emission spectra are sufficiently separated in order to be detected individually.

Green fluorescent protein

Green fluorescent protein (GFP) is a fluorescent protein that occurs naturally in certain cells of the jellyfish *Aequoria Victoria* [47]. This protein can be introduced in cells grown *in vitro*, or in specific cells in a living organism by means of recombinant DNA methods: A gene that codes for GFP is introduced in the DNA of the cell, and results in synthesis of GFP in the cell. These cells are called *GFP transfected cells*, and can be detected with fluorescence microscopy by using filter packages that detect the fluorescence in the green region of the light spectrum.

The unit in GFP that absorbs and emits light is well protected within the compact folded structure, which reduces the probability of de-excitation through non-light-emitting processes as a result of interactions with the surroundings. This makes GFP a robust and stable protein. Several GFP mutant proteins have been produced. These mutants have higher emission than the original GFP and some have also different emission spectra [47].

2.3.3 Microscopic imaging techniques

In microscopy the ability of convex lenses to concentrate light is utilized to form real magnified images of objects that are currently outside the focal plane of the lens. This simple principle forms the basis of a number of advanced imaging systems.

[3] Chemical degradation of a fluorophore resulting in absence of fluorescence [47].

Light microscopy

The main components in a light microscope are the light source, the condenser lens, the objective lens and the eye piece [47]. The light source in a conventional light microscope is usually a halogen bulb that emits white light. The light from this lamp is focused on a small area of the sample by the objective lens. This results in a magnified real image of the object in a image plane as shown in Figure 2.13. Typical magnifications in the objective lens is in the range of 4× to 100×. The image is subsequently magnified by the eye piece, which creates the resulting image on the retina. The total magnification is given by the product of the magnification in the objective lens and the magnification in the eye piece.

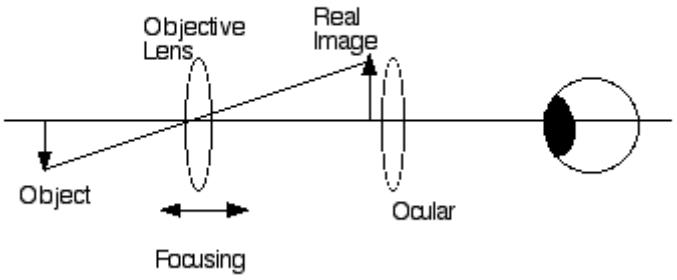

Figure 2.13: Focusing of light by an objective lens results in a magnified real image of the object which can be imaged by the ocular. Adapted from [48].

A modern light microscope usually combines various lenses to improve the magnification and the image quality by correcting lens irregularities and chromatic aberrations. Optimal illumination of the sample is obtained when the sample is evenly illuminated in the field of view, and the sample is illuminated with a cone of light that is as wide as possible. These criteria are fulfilled using Köhlers illumination principle [47].

The lateral resolution d of a microscope is defined as the shortest distance between two points in the object which can be separated to be observed as two separate points in the image. This will be limited by diffraction, and is given by the Rayleigh criteria [47]:

$$d = \frac{0.61\lambda}{NA}, \tag{2.6}$$

where NA is the numerical aperture and λ is the wavelength of light. The numerical aperture is determined by the refraction index n of the media between the sample

and the objective, and the maximal angle θ the light rays can have relatively axis normal on the objective lens and still reach the objective as,

$$NA = n\ sin(\theta). \tag{2.7}$$

The thickness of the slice of the sample that is in focus is given by the axial resolution Z in the objective plane, as

$$Z = \frac{n\lambda}{NA^2}, \tag{2.8}$$

and can be improved with increased magnification in the objective and eye piece.

Inverted microscope

One of the problems in conventional microscopy is the limited working distance between the object table and the objective lens. Objective lenses with magnification in the range of 25× to 40× yield working distances of 3 to 5 mm [48]. Inverted microscopes get an increased workspace since in an inverted microscope the light source and the condenser are located above the object table, and the objective lens is placed under the object table. In addition, gravity will facilitate the imaging, for example in the case of imaging cells in the bottom of growth bottles or Petri dishes. A disadvantage with inverted microscopes is that they have a more complex structure and lower maximum magnification compared to the conventional microscopes.

Fluorescence microscopy

In fluorescence microscopy, a mercury or halogen lamp excites fluorophores in the sample. By using an excitation filter, the wavelength of the light can be adjusted to the excitation wavelength of the used fluorophore. Then the emitted light is detected with a system of filters and dicromatic mirrors that separate the fluorescent light from the excitation light. This separation is possible because, as mentioned before, the fluorescent light have longer wavelength than the excitation light.

An important advantage of fluorescence microscopy is that it gives a high signal-to-noise ratio which permits the detection of low concentrations of the molecule under investigation [47]. In fluorescence microscopy epi-illimination can be used since the fluorescent light has longer wavelengths than the excitation ligh. The sample is then illuminated with excitation light through the same lens that detects the fluorescent signal. The excitation light and the fluorescent light are separated by a dichromatic mirror that only allows light with wavelengths above a specific value to pass through and the rest of the light is reflected.

Chapter 3

Materials and methods

3.1 Experimental schedule

The experiment started with the preparation of the window chambers in the dorsal skinfold of the mice and the spheroids were implanted inside the chamber and the first light and fluorescence microscopy images (GFP images) of the chamber were acquired. This day was considered day zero. From the first light and GFP images of the implanted spheroids, the mice were divided into two groups: one that would be treated with the cyclic hypoxia gassing and the other used as control, attempting to keep both groups without any particular difference, *i.e.*, same number of individuals per group and implanted spheroids of approximately similar sizes between the two groups. Once the two groups were separated the mice were kept in different cages marked with their batch number and if they belonged to the control or the treatment groups.

Table 3.1: Timetable for the experimental procedure.

Day:	**Tasks:**
0	Insertion of window chambers in dorsal skinfold of mice. Implantation of spheroids in chambers for both groups: control and treatment. First GFP and light microscopy pictures of the two groups.
1 to 9*	4 h. cyclic hypoxia exposure to the treatment group. *GFP and light microscopy on days 3 and 7 to assess progression of treatment and control groups.
10	Filming of BST videos and last acquisition of GFP and light microscopy images (treatment + control mice).

As shown in Table 3.1, every day from day 1 to day 9 of the experiment, mice in the treatment group were exposed to 4 hours of cyclic hypoxia. On days 3 and 7, light microscopy and GFP pictures were acquired for each mouse in both, the treated and the control groups. The last day of the experiment was the day 10, on this day the last light and GFP images were acquired and the filming of the videos was effectuated. After completing the video and image acquisition, the mice were sacrificed by neck dislocation before waking up from the anesthesia.

3.2 Cells and multicellular spheroids

A-07 human melanoma cells transfected with green fluorescent protein (GFP) by lipofection were utilized for the experiments. These cells were obtained from a micrometastasis of malign melanoma in a patient at The Norwegian Radium Hospital. Multicellular spheroids of the A-07-GFP cells were generated and maintained by the liquid-overlay assay as in [49].

The tumor cell spheroids were cultivated in T75 cell flasks (Nunc, Denmark) with agar bottom to prevent the cells from sticking to the bottom. Additionally, 30 ml of growth medium was added to each bottle. The medium consisted of 500 ml *RPMI*-medium, plus 75 ml of *BSA*® (E. Pedersen & Sønn, Norway), 2.5 ml of L-glutamin (Invitrogen, Denmark), 5 ml of penicillin/streptomycin (Invitrogen, Denmark) and *Geneticin*® (Invitrogen, Denmark). A gene with antibiotics resistance against geneticin was added to the GFP-gene to prevent the growth of cells without GFP. The cell bottles were placed on a tilt the first 3-4 hours after the seeding. This initiated spheroid growth by helping the cells stick together. The day after the seeding, single cells and longer chains of cells were removed by a pipette and it was added 15 ml of new medium. The spheroids were controlled in a microscope and the medium was changed once a week.

After all the window chambers were implanted in mice, the spheroids were harvested. At the harvest, the spheroids were transferred with a sterile glass pipette to a flask with 10 ml HBBS buffer without $CaCl_2$ or $MgCl_2$ (Invitrogen, Denmark). Then the flask with the spheroids was put on ice to keep them cold until the implantation time.

3.3 Mice

Adult female BALB/c *nu/nu* mice, approximately 8 weeks old, were used for the experiments in this work. These mice were bred at the animal facility at the Norwegian Radium Hospital under specific pathogen-free conditions, at a constant temperature of 25±1°C and humidity of 40±10%. Mice were fed with sterilized food and water *ad libitum*. After implantation of window chambers, mice were transferred to a scantainer cabinet with a constant temperature of 31°C and humidity between 60 and 70% in order to compensate the increased heat loss at the edges of skin surrounding the window chambers.

Breeding, care and experimental procedures were done in accordance to national rules for Laboratory Animal Science as well as with the Interdisciplinary Principles and Guidelines for the Use of Animals in Research, Marketing and Education (New York Academy of Sciences, New York, NY, USA).

3.4 Anesthesia

Before the surgical procedure for the implantation of the window chambers and the spheroids, mice were anesthetized by either *i.p.* or *s.c.* injection of a mixture of *Hypnorm*® (0.315 mg/ml fentanyl citrate and 1 mg/ml fluanisone, Veta Pharma Ltd, UK), and *Dormicum*® (5 mg/ml midazolam, Roche, Switzerland). The proportions for the mixture were one part of *Hypnorm*®, one part of *Dormicum*® and two parts of sterile water, and the dosage of the mixture was 0.008 ml/g of body weight.

After the surgical procedures, the mice received an *i.p.* injection of 0.1 ml of 1:10 dilution in saltwater of the analgesic *Temgesic*® (buprenorphine, Schering-Plough, Brussels, Belgium) which relieved the pain for the posterior 4 to 8 hours.

3.5 Window chamber preparations

Prior to the implantation of the window chambers, the mice were anesthetized as described above. Then their skin was washed carefully with chlorine hexidin, and the mice were placed on a sterile operation cloth. The sagittal center line and the desired axial placement of the chamber were marked on the skin with a pen. Since the vascular network is symmetrical at the sagittal axis, it was assessed that the center line was correctly drawn by lifting the flip of skin on the back, placing the two skin layers against each other until the vascular network in the skin layers

overlapped. In order to fixate the flick of skin for the implantation of the chamber, the dorsal skinfold of mice was sown to an *in-house-made* holder (Produced at the workshop of the Norwegian Radium Hospital) with a surgical silk suture.

A circular perimeter with a diameter of 6 mm (same size of the transparent window) was marked with a pen on one of the sides of the dorsal skinfold. Then, a circular hole in one skin layer was made with a pair of surgical scissors within the marked circular area. This was done to uncover the vascular network on the opposite skin layer. A layer of nerves and fat on the exposed skin was removed in order to obtain a higher quality in the microscopy images. Three holes were made with a punch biopsy cutter evenly distributed around the exposed circular area. These holes were made to attach the two parts of the chamber together with screws. Then the front and back parts of the chambers were assembled, screwed together, and sown to the skin with surgical silk suture, ensuring that skin was not squeezed together so that the blood supply was not altered. Throughout the operation, physiological salt water was used to humidify the skin in the exposed area to prevent drying in the prepared skin layer. After the chamber was sown to the skin, the covering glass was carefully attached checking that air bubbles had not formed under the glass. Then, a rubber ring slightly larger than the glass covering the chamber was placed over the latter with the help of tweezers. An Ω-ring (as the one illustrated in Figure 3.1-Right) was placed with a specially designed set of pliers in order to fix the glass to the chamber. After completing the surgical procedure, the wounds were lubricated with 2% *Fucidin*® (Leo Pharma A/S, Norway) and 0.1 ml *Temgesic*® was injected *i.p.* in the mice to relief possible pain for the next 4-8 hours.

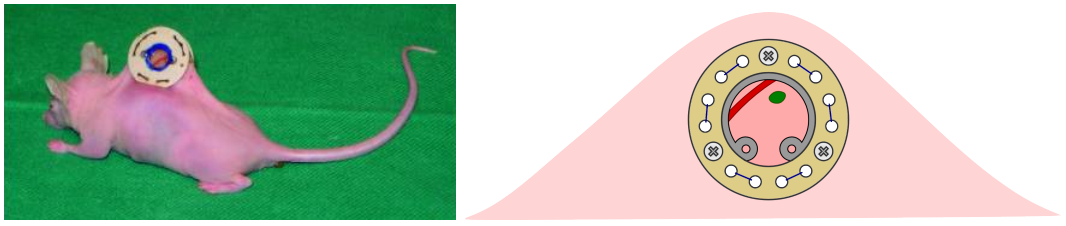

Figure 3.1: **Left:** BALB/c nu/nu mouse with a dorsal intravital chamber. **Right:** Illustration of a dorsal window chamber showing the ideal placement of an spheroid (marked in green) in relation to the reference vessel (marked in red).

The implantation of the spheroids was done immediately after preparing the window chambers. As shown in Figure 3.1, the chambers were placed so that an artery was visible in the periphery of the window. The purpose of this placing was to later use the artery as a reference for calculating the blood supply times in the tumor

vasculature as well as allowing the tumor to grow in the largest possible space within the chamber. The ideal location to implant the spheroid in the window chamber is also illustrated in Figure 3.1-Right. The spheroid is not positioned in the center of the window chamber because it has been observed that the skin have a tendency to lose stiffness and move towards the lower part of the window chamber in previous experiments. A photograph of a mouse carrying a dorsal window chamber is shown in Figure 3.1-Left.

3.6 Hypoxia treatment

The animals in the treatment group were subjected to a 4 hour cyclic hypoxia treatment everyday from day 1 to day 9 of the experiment. The daily treatment consisted of 12 periods of 10 minutes breathing a mixture with 8% oxygen and 92% nitrogen (hypoxia gas mixture), alternating with 10 minutes of breathing normal air. An illustration of the intended changes in oxygen concentration as a function of time is shown in Figure 3.2.

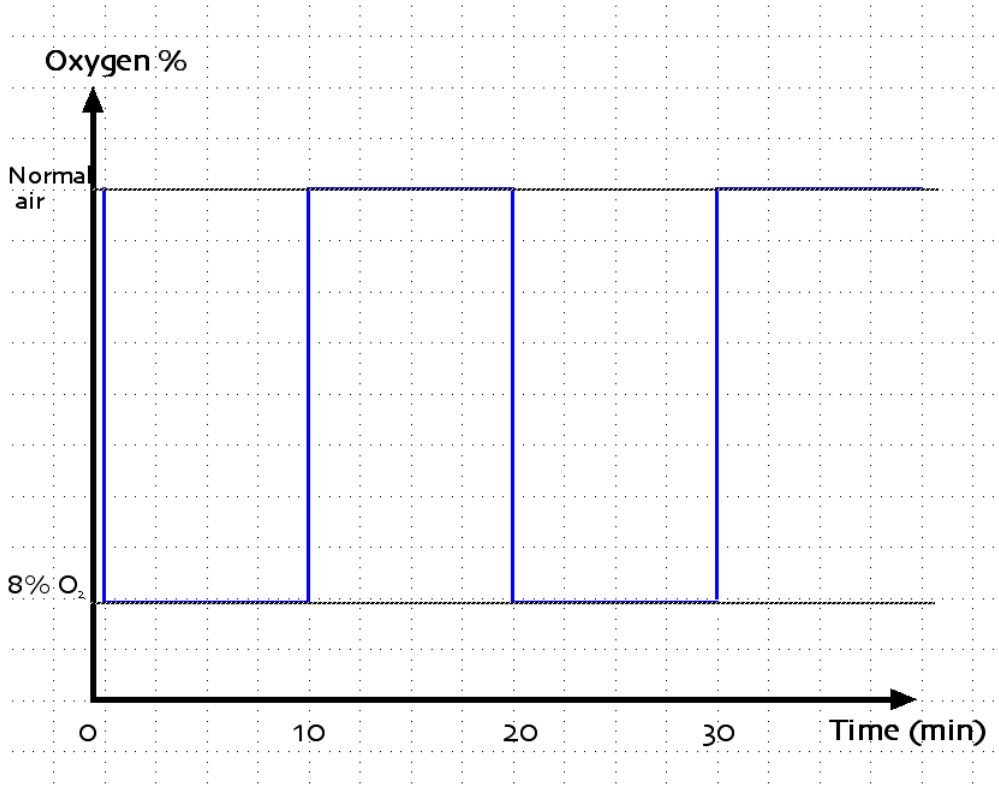

Figure 3.2: Cycles of hypoxia and normal air exposure in the gas chamber. Daily treatment consisted of 12 periods of 10 minutes exposure to 8% oxygen concentration gas alternating with 10 minutes exposure to normal air, giving a daily treatment time of 4 hours. The figure illustrates two of the 12 periods in a daily treatment.

The cycles were regulated by electronically controlled valves. The first valve was open for two minutes to allow the hypoxia gas to flow into the chamber, the valve was then closed for the next 18 minutes. After 10 minutes, the second valve opened for 2 minutes allowing 21% O_2 to fill the chamber. This cycle was repeated for 4 hours.

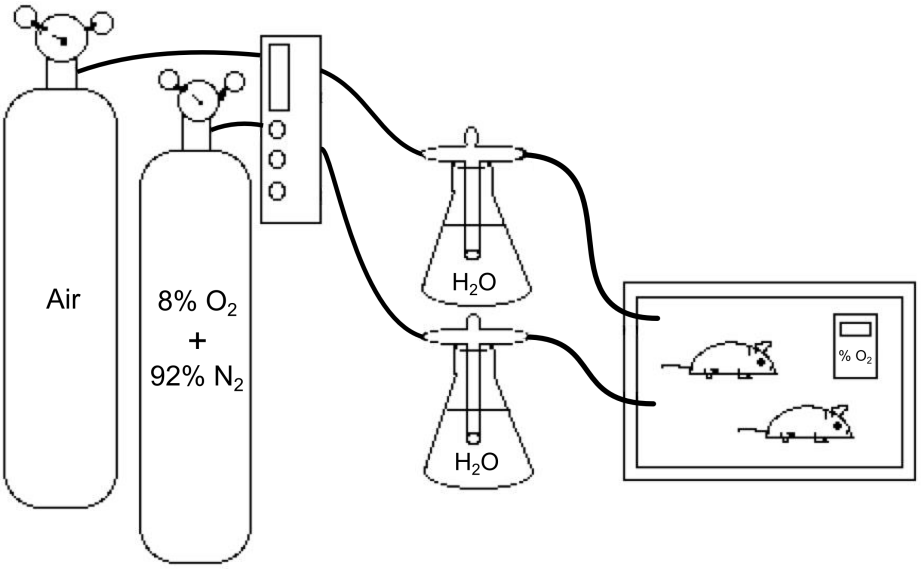

Figure 3.3: Cyclic hypoxia exposure chamber set-up diagram. Electronically controlled valves regulated the inflow of gas. A control-limit was programmed to open and close the valves in order to get the desired hypoxia treatment (Fig. 3.2). The gasses were humidified in flasks with water before continuing their way into the gassing chamber. Inside the chamber, mice were placed in a normal cage, and were allowed to eat and drink *ad libitum*. A device that measured the oxygen concentration in the air was placed inside the gas chamber in order to monitor the oxygen concentration throughout the cycles.

As illustrated in Figure 3.3, both, hypoxia gas and air, were humidified by flushing through flasks with water. This was done in order to prevent irritation due to drying of the mucosa in the mice. The gassing chamber consisted of an *in-house-made* acrylic box. This box had a circular hole with a radius of 1 cm to allow flushing of the gas content when a different gas comes into it. Inside the gas chamber, mice were placed in a normal cage and were allowed to eat and drink *ad libitum*. Additionally, a device that measured the concentration of oxygen was placed inside the gassing chamber to monitor the oxygen concentration throughout the cycles.

3.7 Microscopy imaging

3.7.1 Microscope set-up

An *IX71 Olympus*® inverted microscope (Olympus, Japan) was used for the acquisition of images. The objective lenses used had had a magnification of 2× and 4×. This microscope was equipped a mercury lamp and various filter packages for detection of fluorescent light. GFP-images were taken with the filter package $NIBA$, and TRITC-images with the filter package WIY. The detection system consisted of a black and white *C9300-024 Hamamatsu*® CCD-camera (Hamamatsu Photonics K.K., Japan) and the image acquisition software *WASABI*® (Hamamatsu Photonics K.K., Japan).

While acquiring the images and videos of the tumors, a hot air blower (produced at a workshop in Radiumhospitalet) was used in order to maintain the normal body temperature of the mice by blowing air with a constant temperature of 37°C. The importance of this addition relies on the fact that reduced body temperature not only can affect the mice vitality but also can result in vessel contraction and changes in the blood flow.

3.7.2 First-pass imaging of tumor vasculature

A 0.2 ml bolus of TRITC-dextran (tetra-methylrhodamine isothicyaneate-dextran) of a molecular weight of 155 kDa, diluted to a concentration of 50 mg/ml in physiologic salt water was injected in a lateral tail vein. This bolus was used as vascular tracer for first-pass imaging. The time resolution of the movies was 22.3 fps.

The movie was acquired using the 2× objective in order to include the whole tumor as well as the reference artery in the field of view. Before filming the vasculature, normal light transmission and GFP images were taken. The exposure time chosen for the movie was 40.0 ms, resulting in a combination of exposure time, volume, and concentration of TRITC-dextran that has earlier been shown to give optimal exposure of the movie [50]. During the filming, the lights in the room and the microscope regular lamp were off. After choosing the correct filter for TRITC-dextran, the shutter that blocked the excitation light from the mercury lamp was opened and the video acquisition started as the TRITC-dextran bolus was injected. After filming for 30 seconds, the video acquisition was stopped and the shutter was closed in order to prevent photo bleaching and overheating of the chamber in the mouse.

3.7.3 Morphology images

An objective lens with a 4× magnification was used in order to obtain images of the tumor vasculature with better spatial resolution. However, this resulted in a smaller FOV and for some large tumors more than one image had to be acquired and patched together to cover the entire tumor. The morphology images were acquired immediately after the video filming was completed. Light microscopy was used to focus the image and the choose the FOV. For every tumor or region of it (in the case of large tumors that required more than one image) light microscopy, GFP and TRITC images were acquired. The optimal exposure time was chosen individually for every image. The images were stored in TIFF format (Tagged Image File Format) for further analysis. The image quality control, and the analysis of the intensities in the pixels in every frame was executed using *AquaCosmos*® 2.5 (Hamamatsu Photonics K.K., Japan) software.

3.8 Data analysis

3.8.1 BST

The blood supply time, *BST*, is a functional parameter of the vascular network defined as the time difference between the maximum fluorescence intensity in a pixel inside a blood vessel and the maximum fluorescence intensity in the main supplying artery (MSA) of the tumor.

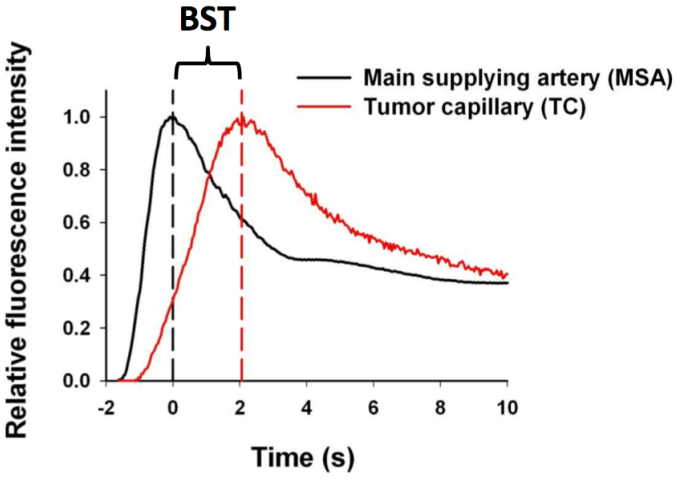

Figure 3.4: BST assignment method. The MSA of the tumor is chosen as reference for the BST in all the pixels of the tumor vasculature: the time difference between the maximum fluorescence intensity in the MSA and the maximum fluorescence intensity in a specified pixel of a capillary will be the BST of that pixel.

Figure 3.4 illustrates the determination of the BST: First, an artery that supplies the tumor is chosen as reference. The time of maximum fluorescent intensity in the MSA is defined $t = 0$. The pixels within the tumor vasculature will have a time of maximum fluorescent intensity a certain time after the MSA. This time difference is defined as BST.

The BST was calculated for every pixel in the image using a program developed in *IDL*® (Interactive Data Language, Research Systems Inc., Boulder, USA) at the Department of Radiation Biology at the Norwegian Radium Hospital. The reference value was determined by calculating the average in a circular ROI in the reference artery. The BST-value was then extracted from all the pixels within the vascular network by applying the vascular mask. The vascular mask was established from a maximum trace image consisting of the maximum fluorescence intensity in each pixel throughout the film [51].

3.8.2 Morphology

For quantitative analysis of the morphology of tumor vascular networks, masks of the vasculature were created. This masks were obtained in *MATLAB*® (The MathWorks, Inc., USA) by running a program developed at the Department of Radiation Biology at the Norwegian Radium Hospital, with the assistance of *Norsk Regnesentral*. The program consists in the application of a *white top-hat* transform, which removes contributions from light background noise, afterwards, the images are eroded with linear structure elements before effectuating local thresholding. This yields a binary image of the vascular network, where the pixels comprised in the vessels are set to 1 and the rest to 0. From the vascular masks the morphological parameters: vascular length density, vascular area fraction, interstitial distance and vessel diameter were calculated by *in-house-made* algorithms developed at the Department of Radiation Biology at the Norwegian Radium Hospital [52].

3.8.3 Tumor growth

The area of the tumors was obtained in *AquaCosmos*® 2.5 (Hamamatsu Photonics K.K., Japan) by manually drawing the tumor perimeter on the GFP-images.

3.8.4 Statistical analysis

The statistical analysis and plotting of the data was effectuated using *SigmaPlot*® (Systat Software Inc., USA) and *MATLAB*® (The MathWorks, Inc., USA). The data was compared by the student t-test using a significance criteria of $p < 0.05$.

Chapter 4

Results

4.1 Oxygen concentration in gas chamber

Before mice were exposed to cyclic hypoxia, the experimental set-up was tested. the desired hypoxia treatment consisted of cycles of 10 minutes exposure to 8% of oxygen alternating with 10 minutes exposure to normal air (20.9% O_2). In order to test the system, a device that measures the oxygen concentration in air was put inside the gas chamber, and the oxygen concentration was recorded for two cycles. This was plotted in Figure 4.1.

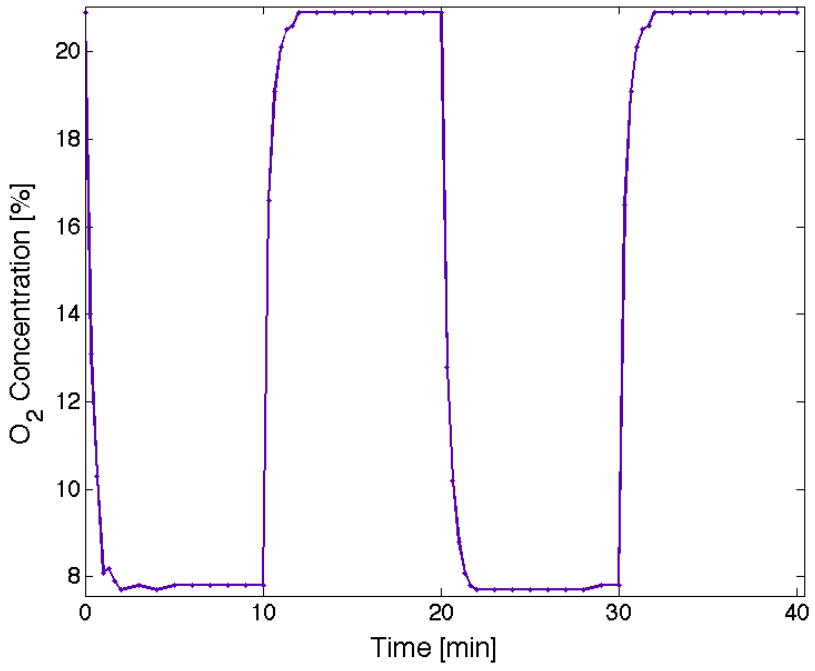

Figure 4.1: Oxygen concentration in the gas chamber as a function of time for two cycles.

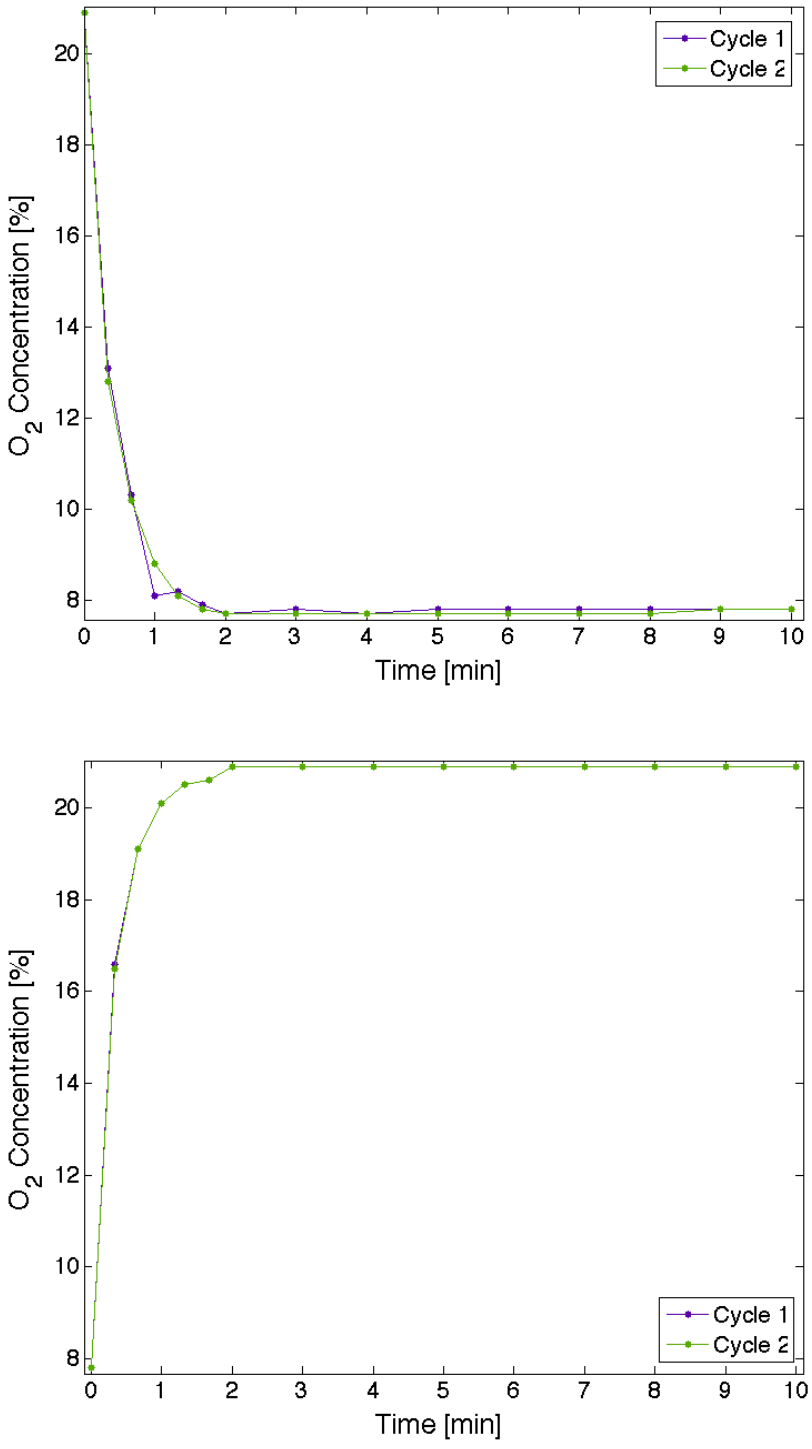

Figure 4.2: **Top:** Concentration of oxygen in the gas chamber as a function of time, during filling of the chamber with hypoxia gas for two minutes and 8 minutes afterwards in two different cycles. **Bottom:** Oxygen concentration in the gas chamber versus time, during filling of the chamber with air for two minutes and 8 minutes afterwards, in two different cycles that followed a period of hypoxia gassing.

Another requirement to be fulfilled was that the cycles in either the hypoxia gas or the air exposure were similar to each other, *i.e.*, that the increase and decrease in the oxygen content inside the chamber for one cycle did not vary significantly for the same process at a different time. For this reason, in Fig. 4.2, two hypoxic and two air gassing cycles were plotted overlapped as a function of time, respectively. From these plots, it is possible to see that the cycles were reproducible and the desired oxygen concentration was reaches approximately one minute after the valves were opened.

4.2 Implanted spheroids

As part of the quality control in this experiment, it was required that the size of the implanted spheroids did not vary significantly between the two groups (both, treatment and control groups consisted of 10 tumors each). Because of this, the area of the implanted spheroids was measured from the first fluorescence microscopy images (GFP images) and plotted in Figure 4.3.

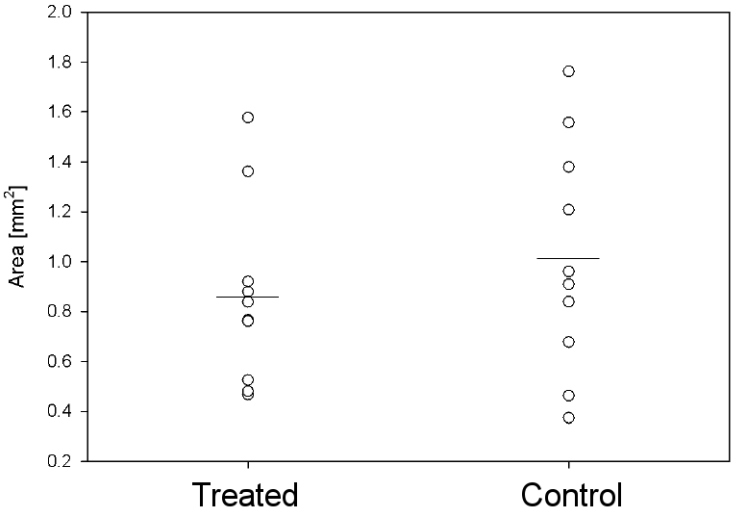

Figure 4.3: Area of the spheroids measured from the GFP images acquired right after their implantation. The horizontal line represents the average in the area of the implanted spheroids for each group. The difference between the treated and control groups was not significant ($p > 0.05$).

Moreover, a student t-test was effectuated to compare the groups. According to the t-test, the difference in size of the implanted spheroids between the two groups was not of statistical significance ($p > 0.05$).

4.3 Tumor growth

Tumor growth was quantified by measuring the area of the tumors from the fluorescence microscopy images (GFP images), since in these ones the contrast given by the GFP makes easier to delimit the tumor.

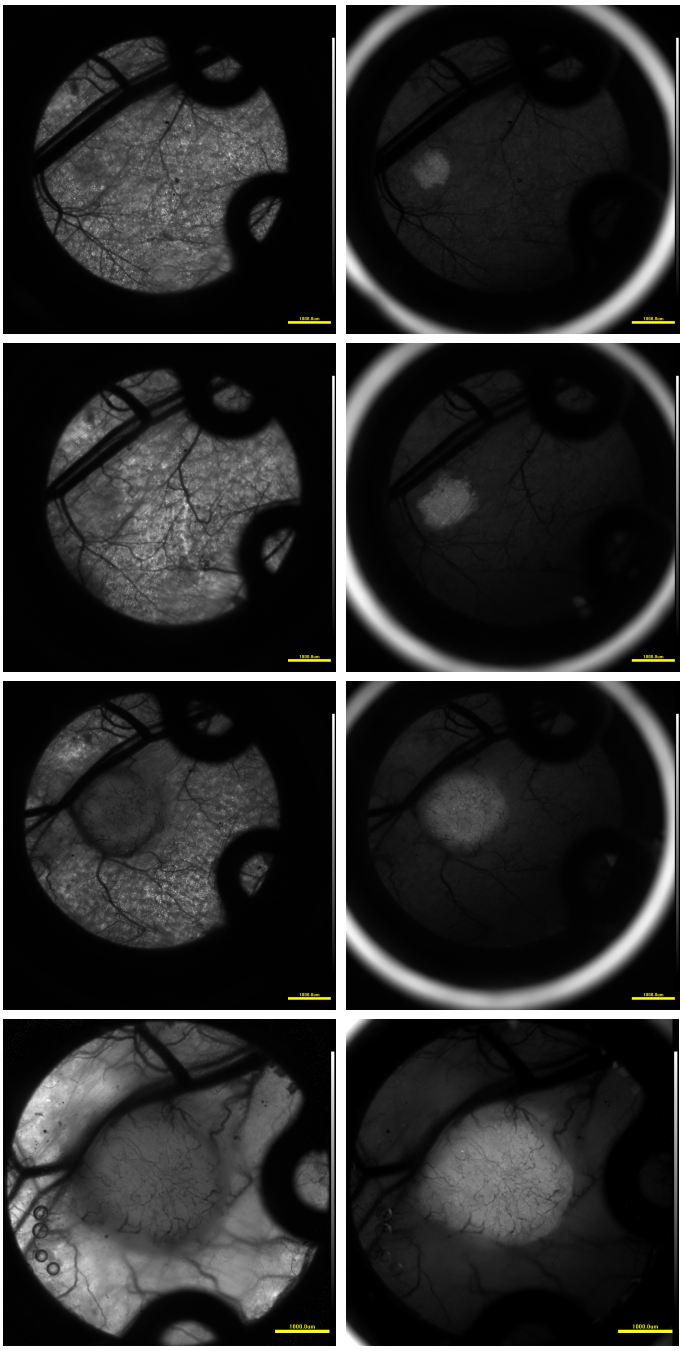

Figure 4.4: **Left panels:** Light microscopy images of a representative treated tumor on days 0, 3, 7 and 10, respectively from top to bottom. **Right panels:** GFP images of the same tumor at the same time than in the picture in the left. The scale bar represents 1 mm.

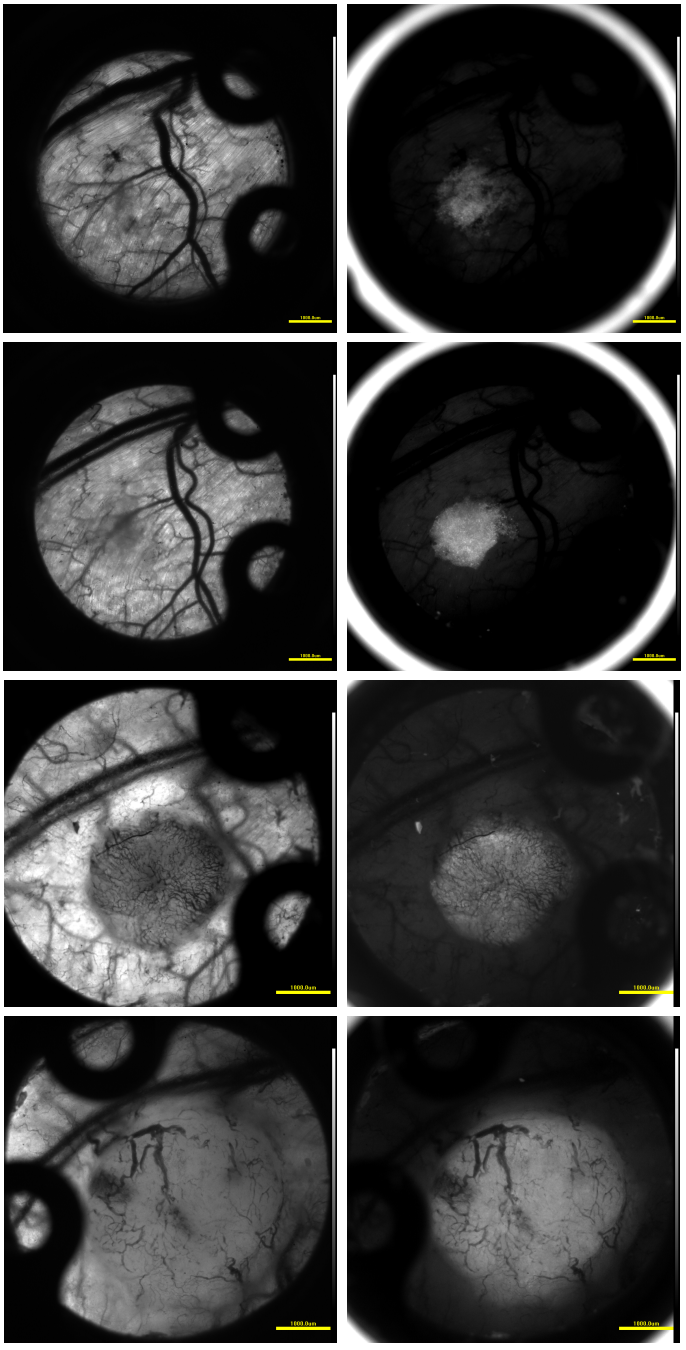

Figure 4.5: **Left panels:** Light microscopy images of a representative control tumor on days 0, 3, 7 and 10, respectively from top to bottom. **Right panels:** GFP images of the same tumor at the same time than in the picture in the left. The scale bar represents 1 mm.

Figure 4.4 shows the growth of a representative treated tumor. In the top part, the light microscopy images are shown. From these, one can see the normal vasculature in the surroundings of the implanted spheroid and how the vessels are slightly moved towards the tumor after this latter has began the angiogenic process. In the GFP images (bottom), is possible to see how the growth rate of the tumor

seems to increase more rapidly with time. The same can be observed in Figure 4.5, where a representative control tumor is shown. However, the control tumors seemed to increase in size faster than the treated ones. In order to get a more objective appreciation of these apparent differences in growth rate, the size of the control and the treated tumors was plotted as a function of time as presented in Figure 4.6.

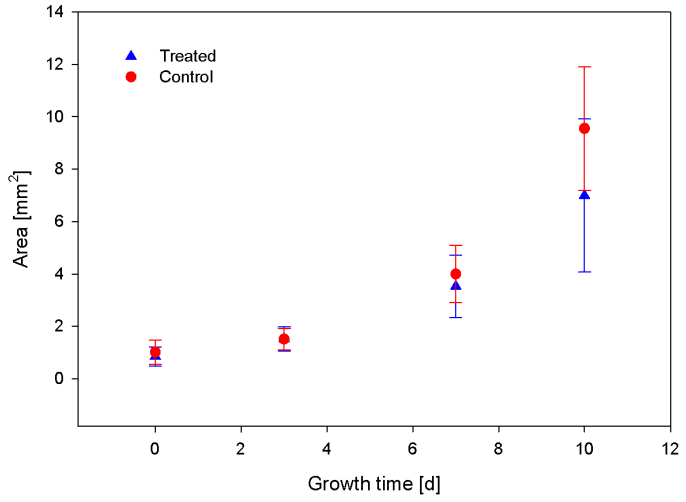

Figure 4.6: Tumor area of treated and control tumors from the day the spheroids were implanted in the window chambers until the last day of the experiment. Each point represents the mean of 10 tumors, and the error bars correspond to the standard error of the sample.

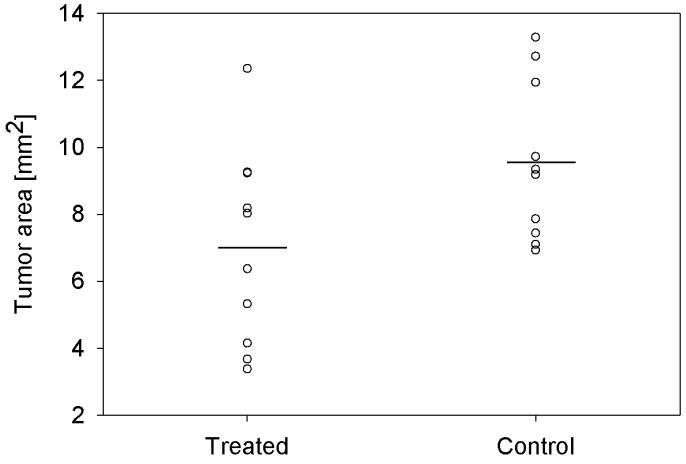

Figure 4.7: Tumor area at the end of the experiments for treated and control tumors. The horizontal line represents the average value of the tumor size for each group (~ 6.99 mm^2 for the treated tumors and ~ 9.55 mm^2 for the control tumors). The difference between the growth in the two groups is significant ($p = 0.045$).

To confirm if the tendency in the growth rate difference was significant, tumor area of the treated and control tumors at the last day of the experiments was plotted and is shown in Figure 4.7. The student t-test was used to compare both groups and yielded a p-value of $p = 0.045$, therefore, the differences in tumor area at the end of the experiment between the treated tumors (6.99 ± 2.91 mm^2) and control tumors (9.55 ± 2.35 mm^2) was statistically significant.

4.4 Vascular morphology

The vascular masks produced from high-resolution images of the tumors (×4 objective lens) as binary images. Since the parameters describing the tumor vascular morphology were computed from these masks, it was important to verify that the masks kept indeed the characteristics of the vascular network in the tumor.

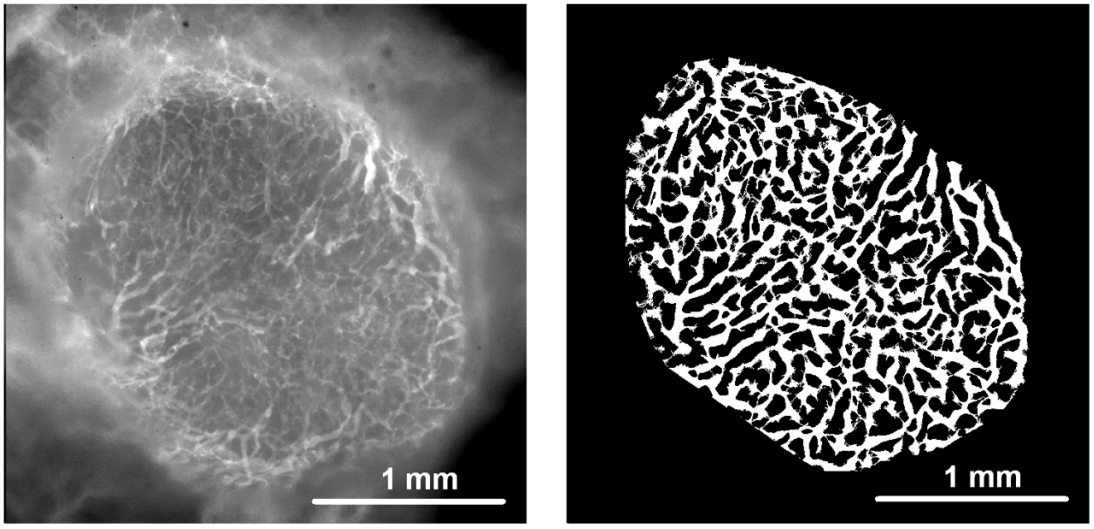

Figure 4.8: **Left:** TRITC-dextran intravital microscopy image of a representative treated tumor acquired with a ×4 objective lens. **Right:** Mask of the vascular network of the same tumor produced from the TRITC-dextran image.

Figures 4.8 and 4.9 show the vascular networks of representative treated and control tumors, respectively. In the left side, the TRITC-dextran images of the tumors are shown and in the right side, the binary mask of the tumor vasculature. From these images, heterogeneities in vessel density are noticeable, with apparent higher density in the periphery than in the center of the tumor, this is specially evident in the control tumor (Fig. 4.9). These heterogeneities in vessel density are quantified in the following section. The general quality of the vascular masks was comparable to that of the tumors shown these images.

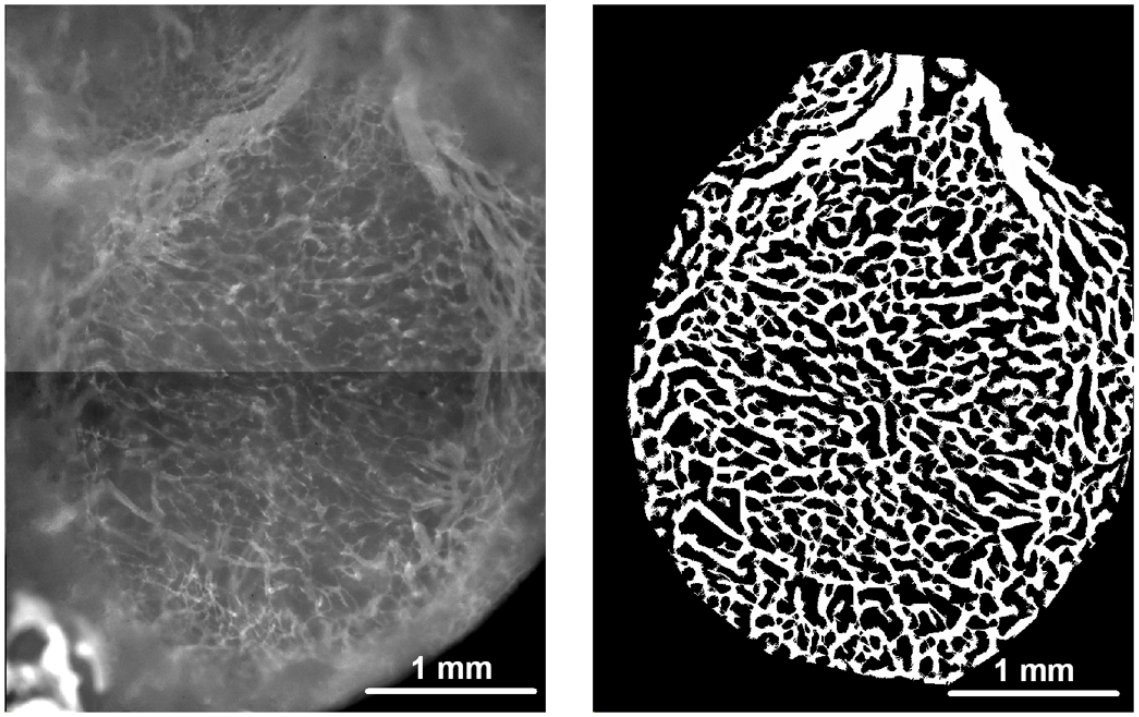

Figure 4.9: **Left:** TRITC-dextran intravital microscopy image of a representative control tumor acquired with a ×4 objective lens. **Right:** Mask of the vascular network of the same tumor produced from the TRITC-dextran image.

4.4.1 Vessel density

The vessel density parameters calculated from the tumor vascular masks were the vascular length density, the vascular area fraction and the interstitial distance.

Vascular length density

The vascular length density is a parameter of the microvascular density in the tumor defined as the total vessel length per μm^2 of tumor area. Figure 4.10 shows the results of computing the vascular length density in the tumors treated with cyclic hypoxia and the control tumors. From this plot, a trend towards higher vascular length density in the treated tumors is evident, however, the comparison of the two data groups yielded a p-value of $p = 0.194$, and thus, the difference can not be considered significant. The vascular length density in the treated tumors ranged from $\sim$0.018 to $\sim$0.025 $\mu m/\mu m^2$, with an average value of 0.0214 ± 0.0021 $\mu m/\mu m^2$; whereas the control tumors had vascular length densities between $\sim$0.0178 and $\sim$0.0238 $\mu m/\mu m^2$ and had an average value of 0.0202 ± 0.0018 $\mu m/\mu m^2$.

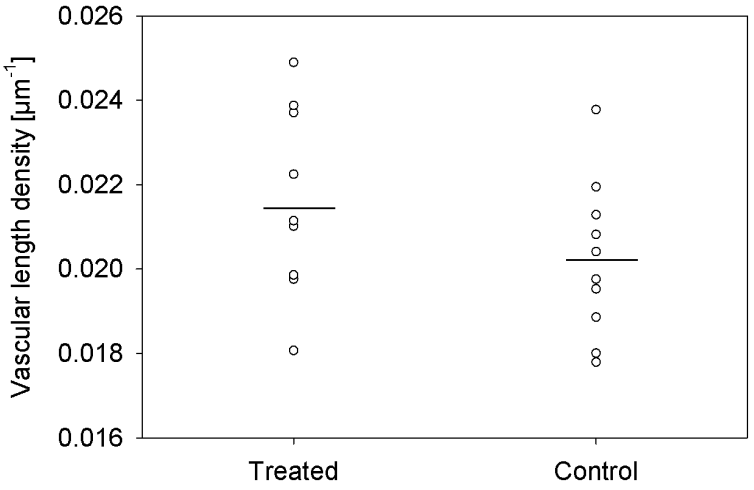

Figure 4.10: Vascular length density of the treated and control tumors. The horizontal lines represent the average values ($\sim$0.214 μm/μm^2 and $\sim$0.0202 μm/μm^2 for the treated and the control tumors, respectively). The difference between the two groups of tumors was not statistically significant for this parameter ($p > 0.05$) in spite a trend towards higher values in treated tumors.

Vascular area fraction

The vascular area fraction (VAF) is a dimensionless parameter of the vascular density in the tumor defined as the ratio of the number of pixels within the vascular mask to the total of pixels comprised in the tumor area.

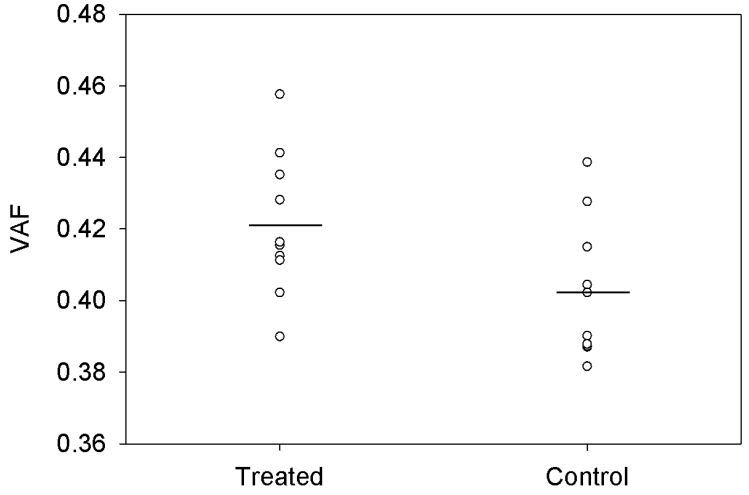

Figure 4.11: Vascular area fraction (VAF) of the treated and control tumors. The horizontal lines mark the average values ($\sim$0.421 and $\sim$0.402 for treated and control tumors, respectively). The difference in the VAF between the two groups of tumors was statistically significant ($p = 0.046$).

Figure 4.11 shows the vascular area fraction of tumors that were exposed to cyclic hypoxia treatment and control tumors. The treated tumors had vascular area fractions between ∼0.389 and ∼0.457, and an average of 0.421 ± 0.019. Conversely, the control tumors had vascular area fractions ranging from ∼0.381 to ∼0.438, with a mean value at 0.402 ± 0.019. The p-value obtained from the t-test was $p = 0.046$, hence, it can be said that the VAF in the treated is significantly different from the VAF in the control tumors. This indicates that tumors subjected to cyclic hypoxia developed vascular networks with higher vessel density than the tumors under normal conditions.

Interstitial distance

The interstitial distance was defined as the average distance from a pixel in the tumor that does not belong to the vascular network to the closest pixel inside the vascular mask. Figure 4.12 shows the mean interstitial distances in treated and control tumors. The tumors in the mice subjected to the cyclic hypoxia treatment showed significantly shorter interstitial distances than the tumors in the control group, with a p-value of $p = 0.034$. The interstitial distances in the treated tumors ranged from ∼12.4 μm to ∼16.4 μm with the mean value of 14.2 ± 1.2 μm. The control tumors though had interstitial distances ranging from ∼13.9 μm to ∼19.0 μm, with a mean value of 15.7 ± 1.3 μm.

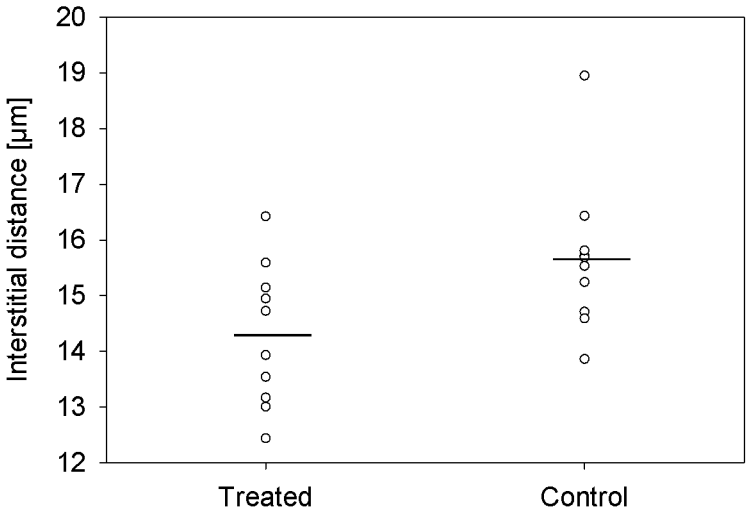

Figure 4.12: Interstitial distance in the vascular networks of the treated and control tumors. The horizontal lines correspond to the average values (∼14.2 μm and ∼15.7 μm for the treated and the control tumors, respectively). The difference in the interstitial distance between the two groups of tumors was statistically significant ($p = 0.034$).

Figure 4.12 indicates that the vessels in the tumors that were exposed to the cyclic changes in oxygen tension were more closer together than the vessels in the control tumors.

4.4.2 Vessel diameter

The vessel diameter of the tumors was calculated as the average of the diameters of all the vessels in the vascular mask. This is plotted in Figure 4.13 for the treated and the control tumors. There was no significant difference between the treated and control tumors ($p = 0.791$) and no clear trend was noticeable. However, the mean values of vessel diameter were more spread for the treated tumors, ranging from ∼20.68 to ∼26.11 μm, whereas the control tumors ranged in vessel diameters from ∼21.52 to ∼25.27 μm. The average values of the vessel diameter were 23.27 ± 1.7 μm for the tumors treated with cyclic hypoxia and 23.46 ± 1.42 μm for the control tumors.

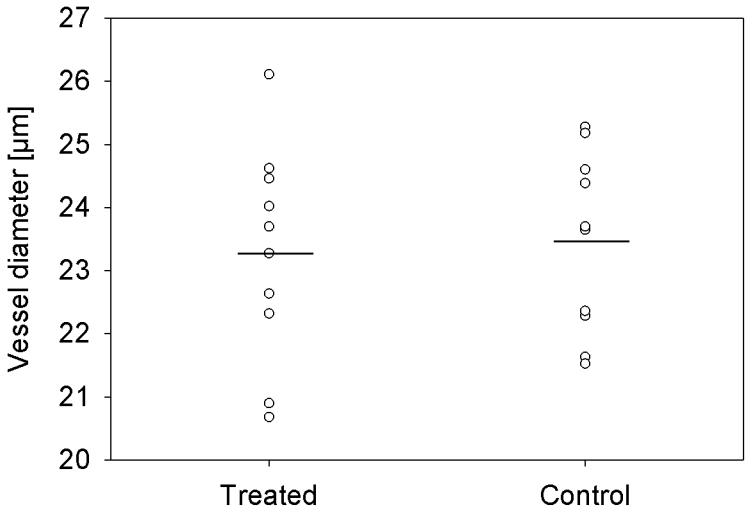

Figure 4.13: Mean vessel diameter in the treated and control tumors. The horizontal lines represent the average values (∼23.27 μm and ∼23.46 μm for the treated and the control tumors, respectively). There was no significant difference between the two groups of tumors ($p > 0.05$).

4.4.3 Intratumor heterogeneity

It was observed that most of the control tumors displayed spatial heterogeneities in the vessel densities, tending to a lower vascular density in the central region. This tendency was not so clear in the hypoxia treated tumors. The tumors were divided into two concentric regions of interest (ROIs) delimited by lines traced at distances

of $2R/3$ and R from the center of the tumor, where R is the radius[1] of the tumor. An example of this division into peripheral and central ROIs of the morphology images of the tumors is shown in Figure 4.14.

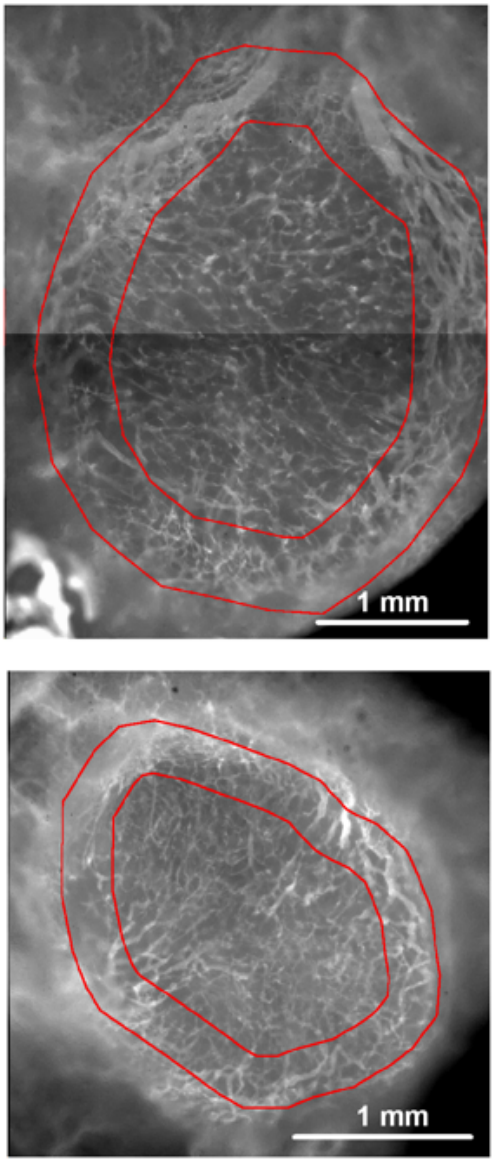

Figure 4.14: Division of the morphology images of the tumors into two ROIs: a central ROI delimited by a line drawn at $2R/3$ and a peripheral ROI between the lines at $2R/3$ and at R, where R is the tumor radius. **Top:** TRITC-dextran image acquired with a $\times 4$ objective lens of a tumor in the control group showing the division of the ROIs. **Bottom:** TRITC-dextran image acquired with a $\times 4$ objective lens of a tumor subjected to cyclic hypoxia treatment, showing the division of the concentrical ROIs.

[1] At a certain angle in a polar coordinate system with origin in the tumor center.

Vascular area fraction in the central ROI

The vascular area fraction in the center of the treated and control tumors is plotted in Figure 4.15, where it is evident that the tumors in the mice subjected to the cyclic hypoxia treatment had higher VAF in this ROI (0.414 ± 0.02) than the control tumors (0.394 ± 0.016). These differences were statistically significant, with a p-value of $p = 0.032$. This difference in vessel density was larger for the central ROI than for the entire tumor (lower p-value $p = 0.032$ *vs.* $p = 0.046$).

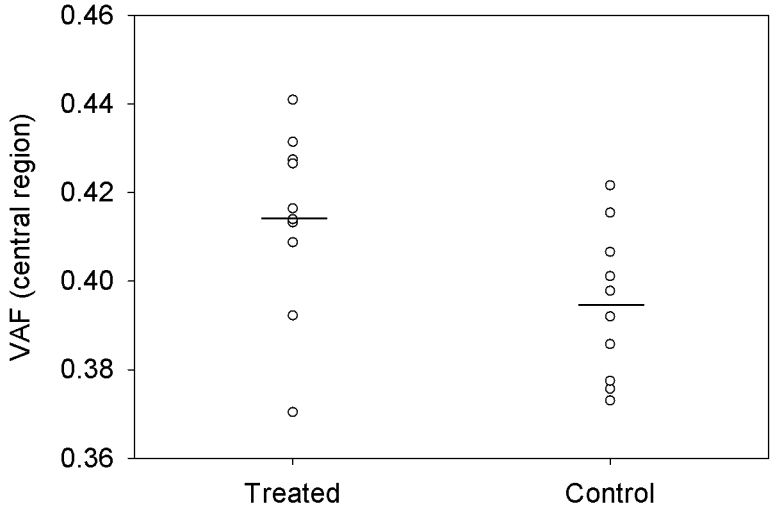

Figure 4.15: Vascular area fraction in treated and control tumors in the central ROI. The horizontal line corresponds to the mean values (0.414 and 0.394 for the treated and control tumors, respectively). The difference between the two groups was statistically significant ($p = 0.032$).

Vascular area fraction in the peripheral ROI

The peripheral ROI comprised the area within $2R/3$ and R of the tumor. The vascular area fraction in the peripheral ROI of the tumors that underwent the cyclic hypoxia treatment and the control tumors is shown in Figure 4.16.

The results show a tendency to higher VAF in the periphery of the treated tumors (with an average of 0.418 ± 0.0148) than in the periphery of the control tumors (average value of 0.408 ± 0.020), however, the difference was not statistically significant ($p = 0.225$). It is also noticeable from both, the plot and the standard errors, that the values of the VAF in this ROI had a larger spread for the control tumors than in the treated tumors. The difference in vessel density was smaller for the peripheral ROI than for the entire tumor (higher p-value $p = 0.225$ *vs* $p = 0.046$).

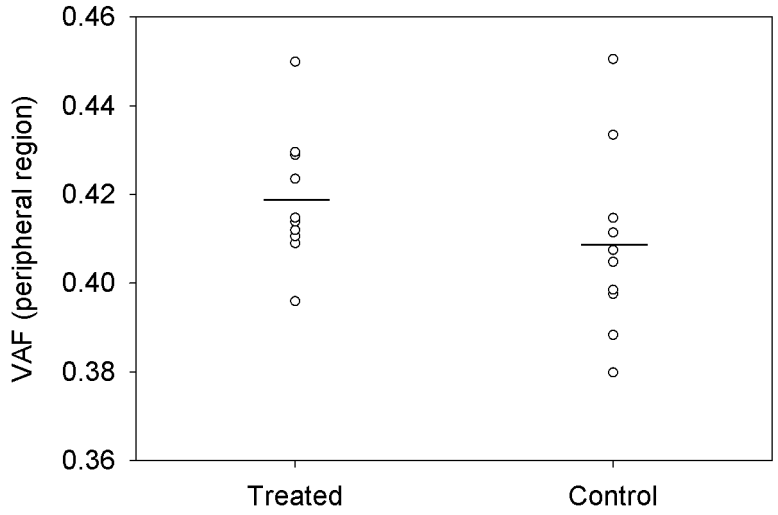

Figure 4.16: Vascular area fraction in cyclic hypoxia treated and control tumors for peripheral ROI. The horizontal line corresponds to the mean values (∼0.418 and ∼0.408 for the treated and control tumors, respectively). There was no significant difference in the VAF for the peripheral ROI between the two groups of tumors ($p > 0.05$), yet, a tendency towards higher VAF in the periphery of treated tumors is apparent.

Hence, tumors treated with cyclic hypoxia developed a more homogeneous vasculature throughout the whole tumor than the control tumors.

4.5 Vascular function

4.5.1 BST

The top panels of Figure 4.17 show frames of a first pass imaging movie of a tumor. The frames correspond to ∼1, 3 and 15 seconds after *i.v.* injection of the TRITC-dextran bolus in the mouse. In the three frames, the main supplying artery (MSA), a tumor arteriole (TA), a tumor capillary (TC) and a tumor venule (TV) are marked. The relative fluorescence intensity of the selected pixels corresponding to the MSA, TA, TC and TV was plotted as a function of time (Fig. 4.17, lower panel). All the vessels showed well-defined peaks in the fluorescence intensity *vs.* time curves, and the time of maximum fluorescence intensity varied among the different vessels, corresponding to different blood supply times (BST).

BST maps and histograms

Once all the pixels in the vascular network of the tumors have a BST-value assigned, color BST maps can be produced by representing the time scale as a color

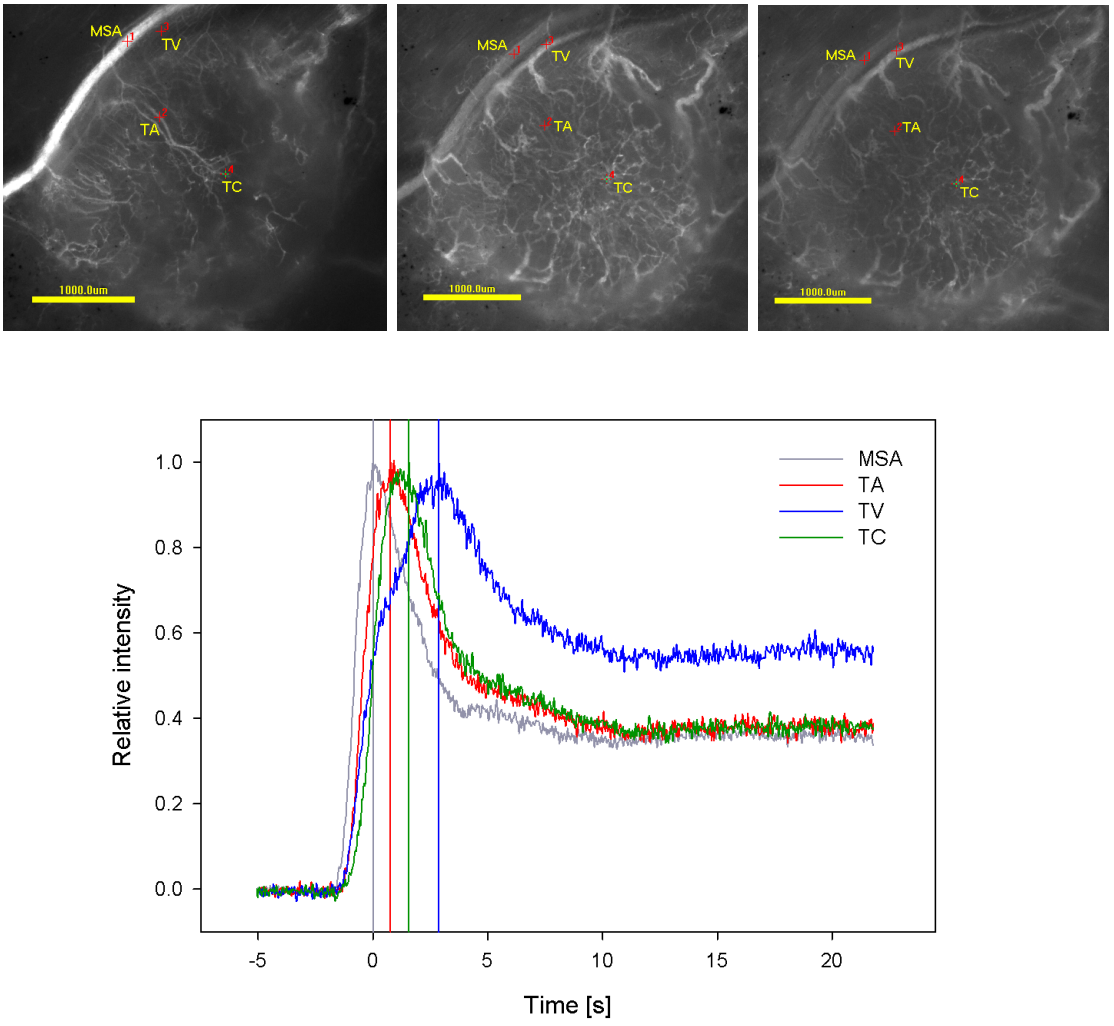

Figure 4.17: Blood supply times of different vessels in a tumor. **Top panels:** Frames of a first pass imaging of a tumor corresponding to approximately 1, 3 and 15 seconds after injection of the TRITC-dextran bolus respectively. The main supplying artery (MSA), a tumor arteriole (TA), a tumor capillary (TC) and a tumor venule (TV) are marked on the frames. The scale bars in all the frames represent 1mm. **Bottom:** Relative fluorescence intensity of the selected pixels (marked in the images) as a function of time. The time scale has been adjusted to make $t = 0$ when the MSA has its maximum fluorescence intensity.

scale. This is shown in the left panels of Figures 4.18 and 4.19, where the red color indicates low BST values in the pixels whereas the blue color correspond to pixels with high BST values.

It was observed that the tumors in the mice subjected to cyclic hypoxia displayed larger variations in BSTs, as shown in the left panels of Figures 4.18 and 4.19. Thess heterogeneities can be better appreciated in the histograms of the BST values in all the pixels of the vascular networks (see the right panel of Figures 4.18 and 4.19). The broader the histogram, the more heterogeneous the tumor is in BST.

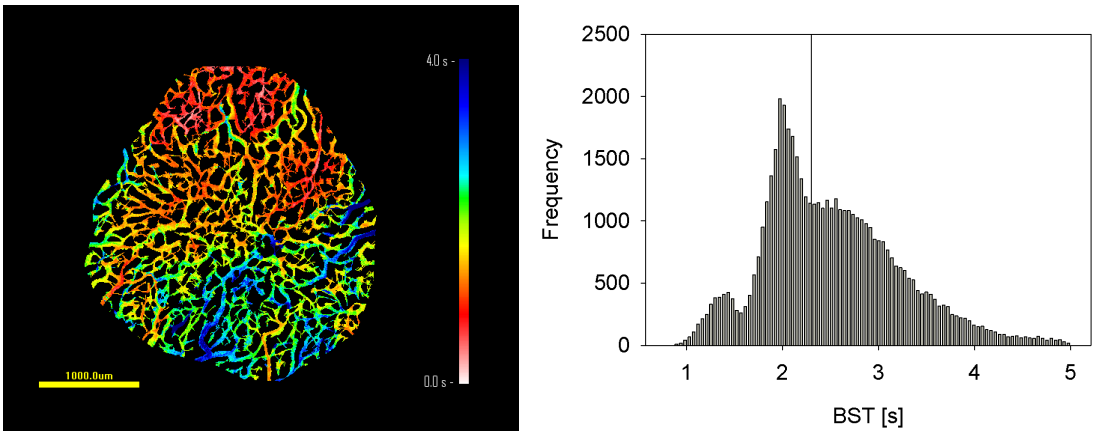

Figure 4.18: **Left:** Blood supply map of a representative treated tumor. The timescale, symbolized by the colorscale, is linear and ranges from 0.0 to 4.0 seconds. The scale bar corresponds to 1 mm. **Right:** Histogram of the blood supply times in this tumor, the vertical bar corresponds to the median BST ($\sim$ 2.15 s).

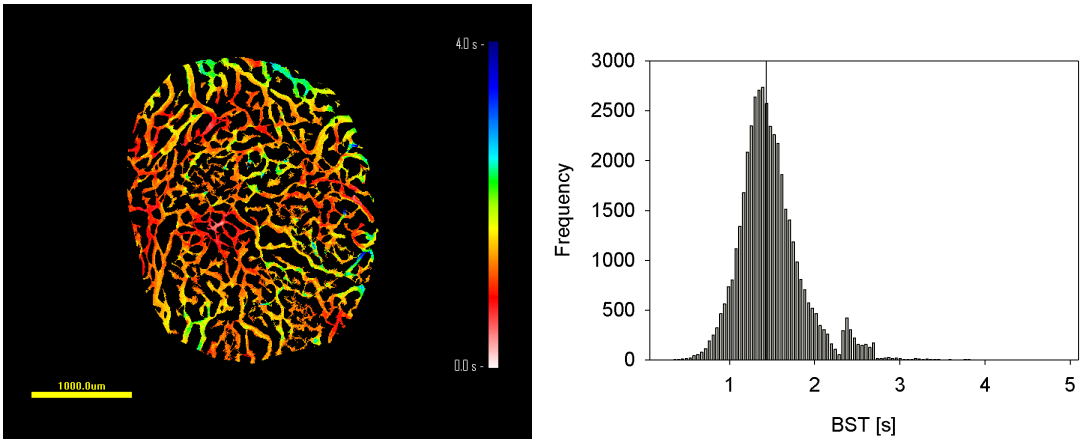

Figure 4.19: **Left:** Blood supply map of a representative control tumor. The timescale, symbolized by the colorscale, is linear and ranges from 0.0 to 4.0 seconds. The scale bar corresponds to 1 mm. **Right:** Histogram of the blood supply times in this tumor, the vertical bar corresponds to the median BST ($\sim$ 1.4 s).

A BST map of a control tumor is shown in Figure 4.19-Left. This tumor is representative among the control tumors in the fact that the vascular network was more efficient, *i.e.* the transit of the bolus of TRITC-dextran not only occurred faster, but also presented less variations throughout the tumor. This reduced heterogeneity was verified in the histogram (Fig. 4.19-Right), where a well defined peak appears around the median value of the BSTs within the vasculature of this tumor.

BST in treated and control tumors

Lastly, the median values of the BST in each tumor of the cyclic hypoxia treated and control groups was plotted, as shown in Figure 4.20. The median BST values in the tumors treated with cyclic hypoxia ranged from 1.25 to 2.40 seconds, and the median BST in the control tumors ranged from 0.85 to 2.19 seconds. The mean values of the BST medians in the tumors were 1.94 ± 0.51 and 1.51 ± 0.56 seconds for the treated and the control tumors, respectively.

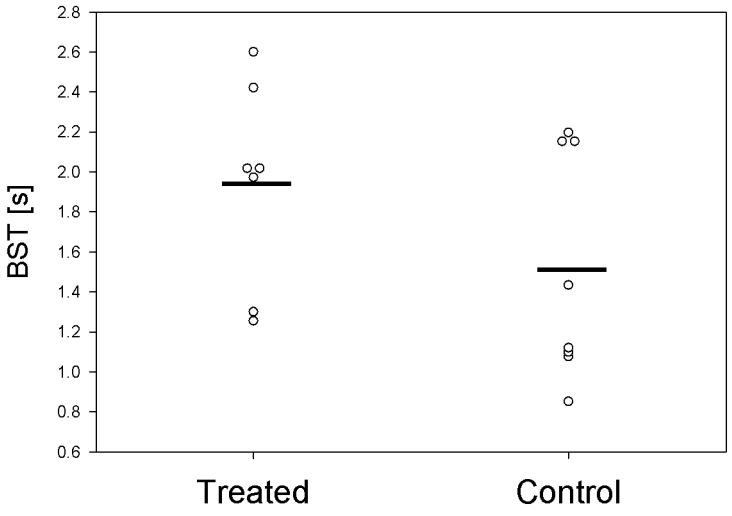

Figure 4.20: BST median values for the treated and control tumors. The horizontal bar corresponds to the mean value of the BST medians in the treated (1.94 s.) and the control (1.51 s.) tumors. A tendency to higher BST values in the treated tumors was visible, however the difference was not statistically significant ($p = 0.148$).

From Figure 4.20, it is noticeable a tendency towards higher BST values in the tumors that were subjected to cyclic hypoxia. Nevertheless, this apparent difference between the treated and control tumor groups was not statistically significant ($p = 0.148$).

Chapter 5

Discussion

5.1 Discussion of materials and methods

5.1.1 Tumor model

Xenografts

The experiments in this work were effectuated on immunodeficient mice with human melanoma xenografts. One of the limitations of using xenografts in research is that after the implantation of the cells in the animal, the vascular network in the tumor will be recruited from the host animal. This might be a problem when interpreting parameters related to the features of the vasculature since blood vessels in the host animal can respond differently to the disrupted balance between angiogenic inhibitors and stimulators. Another important limitation when using xenografts in cancer research is that the immunodeficiency of the host animal is a factor that can permit greater tumor growth rates than in individuals with a normal immunological system. This increase in tumor growth rate could be an advantage experimentally since the experiments can be terminated in shorter time. Yet, the increased growth rate in tumors can influence the development of the vascularity, and the results on experiments that are sensitive to tumor growth rates [29].

In spite of the limitations, xenografts can provide valuable information of the vascularity and blood flow in tumors. There is evidence that xenografts can be adequate tumor models, for example, Rofstad showed that xenografts maintain the histological characteristics from the original tumor [44]. Moreover, the response to radiation therapy, chemotherapy and hyperthermia in xenografts is similar to the response in the original human tumors [29, 44].

Cell line and spheroids

Multicellular spheroids of A-07-GFP cells were implanted in the window chambers in the mice. The sizes of the implanted spheroids varied from one mouse to another, however, it was supervised that at the moment of dividing the mice in the control and treatment groups, the differences in the implanted spheroid sizes were not significant. This was done to ensure that the observations in growth rate between the two groups of mice were not affected by the differences in the sizes of the spheroids.

A limitation with the use of spheroids is that, in order to emulate spontaneous tumors that arise from a single mutated cell, spheroids should contain very few cells. However, smaller spheroids are more likely to be rejected through immune reactions in the host animals. This can happen even in immunodeficient animals.

Since it was wanted to observe the effects of cyclic hypoxia in the tumors, it was important to discard the presence of diffusion-limited hypoxia in this tumor cell line. This has been demonstrated by analyzing histological sections of A-07-GFP tumors extirpated from the mice and dissected after injection of pimonidazole (a well-known chronic hypoxia marker), and by comparing the radiation survival curves of the same cell line irradiated *in vitro* under aerated conditions and the cells in tumors of this same line irradiated *in vivo*. It was demonstrated by the two methods that A-07-GFP tumors of under 100 mm^3 of size (such as those used in this Master Thesis experiments) do not present regions of chronic hypoxia [6].

Window chambers

The use of window chamber preparations has provided valuable information in previous studies of blood flow in experimental tumors [46, 52, 53]. Nevertheless, there are limitations with this method. One of these is the spatial restriction impeding tumor growth in the direction of the window. It is important to notice that even though, there is no spatial restriction in the back side of the chamber, the growth of the tumor as a whole is affected, resulting in hemispherical tumors. Another limitation is that as the tumor grows inside the window chamber and approaches to the size of the window, the tumor will suffer an increased pressure which could result in a reduced growth rate, among other possible consequences.

On the other hand, some of the advantages of the use of tumor window chambers are that the windows permit the observation with microscopes of the vasculature in the tumor. By using window chambers it is possible to monitor the tumor growth rate as well as the development of the vascular network of the tumor with time.

Window chambers also allow the acquisition of movies of the vascular function in the tumors.

In these experiments, the window chambers were implanted in a position that located an artery close to the edge of the window so that the tumor had sufficient space to grow and that the artery appeared in the images and movies. Another important detail is that the experiment was planned taking into account usual growth rates in the used tumor line, in order to prevent tumor growth outside the field of view.

5.1.2 Cyclic hypoxia treatment

The animals in the treatment group were subjected to a 4 hour daily cyclic hypoxia treatment. Each daily treatment consisted of 12 cycles of 10 minutes of only 8% O_2 in N_2 followed by 10 minutes of air breathing. This treatment was received for 9 days starting at the day after the implantation of the window chambers and spheroids.

One of the reasons for choosing this schedule for the cyclic hypoxia treatment is that it has been used previously for investigating the effects of cyclic hypoxia in different tumor models [3, 4, 6]. (The 4 hour treatment choice is related to application of oxic stress in the tumor but prevention of adaptation to this fluctuations in the animal [3].)

In addition, it has been shown that spontaneous fluctuations in oxygen concentrations occur cyclicly in experimental tumors, and that the duration of these cyclic hypoxia periods ranges from less than one minute to several hours [25, 54]. This indicates that a choice of 10 minute periods of hypoxia gas exposure alternating with 10 minutes of exposure to normal air is within a realistic range of what occurs spontaneously in tumors that have not been subjected to hypoxia treatment.

In these experiments, the concentration of oxygen during the hypoxic periods was chosen to be 8%. The exposure to this oxygen concentration is not dangerous for the mice. In other experimental studies of the effects of cyclic hypoxia, mice have been exposed to lower O_2 concentrations during the hypoxic cycles, between 5-7% of oxygen [3, 4, 55]. Rofstad *et al.* measured the oxygen concentration in tumors with OxyLite probes during a cyclic hypoxia treatment identical to that used for this thesis work, revealing that the exposure to 8% of O_2 in the mice resulted in a concentration of oxygen inside the tumor of 0% disregarding if the tumors were

well- or poorly-oxygenated under normal conditions [6]. Thus, it has been proven that exposure to 8% of oxygen induces hypoxia in tumors.

5.1.3 Vascular masks

Vascular masks for quantification of vascular morphology were produced from the TRITC-dextran fluorescence images acquired with a ×4 objective lens with a conventional microscope (described in Chapter 3). One limitation of imaging the tumors with a conventional microscope is that this type of microscopes will get in focus only a slice of the tumor, and all the regions that do not belong to this slice will appear blurred thereby introducing background noise and giving a reduced contrast in the image. This will happen because the tumors are three-dimensional. The thickness of the slice of the tumor that is in focus in the image depends on the wavelength of the fluorescent light, as well as the absorption and emission properties of the tissue.

The use of a conventional microscope results in a projection of a 3-dimensional vascular network into a 2-dimensional image. The contributions from the regions out of the focus introduce uncertainty in the vascular masks and in the parameters calculated from these masks. A consequence of looking at different depths of the tumor simultaneously in the vascular masks could be an overestimated vessel density. One possibility to avoid the projection of the whole tumor in two dimensions would be to use a confocal microscope for the acquisition of the images. This limitation would not occur with a confocal microscope since this type of microscopes only allow the fluorescent light from the selected slice to reach the detector [47].

In spite of these limitations in the vascular masks, the noise was comparable to what has been published previously by Gaustad *et al.* [52]. In this study it was shown that vascular masks calculated by the same algorithm as used in this thesis were comparable to the tumor vascular networks. In addition, as quality control for the vascular masks, the similarity of the mask to the vascular network of the tumor was assessed individually. Those vascular masks that presented regions that did not reproduce the vessels in the tumor were corrected manually.

5.1.4 Calculation of BST

TRITC-dextran injected intravenously was used as a contrast agent for the first-pass imaging of the tumors. A requirement that needed to be fulfilled for the calculation of BST in the studied tumors was to get narrow and well-defined peaks

of the fluorescence intensity versus time curves in every pixel. To achieve this, TRITC-dextran needed to be injected fast, as a bolus. It is known though that fast intravenous injections can result in a temporary increased blood pressure. However, since the bolus was injected into a lateral tail vein, it is possible to assume that before the bolus reaches the vascular network, the pressure in the blood is equilibrated, and that this increase is not significant when the bolus gets into the tumor vasculature. One parameter that is hard to control is the time it takes to inject the bolus. This injection time is most likely to have varied from one tumor to another, thereby affecting the quality of the fluorescence intensity peaks. However, this variations are expected to be small.

It has been shown in previous experiments that this BST calculation method has a fine sensitivity when using a bolus of TRITC-dextran with the same characteristics as the one used in this work [51]. As shown in the lower panel of Figure 4.17 the passing of the bolus in different vessels (main supplying artery, tumor arteriole, tumor capillary and tumor venule) could be detected as well-defined fluorescence intensity peaks. This means that the bolus can be followed in all the different vessels, and therefore, it is possible to obtain BST values in all the pixels comprised in the vasculature of the tumors.

A limitation of the BST parameter is that it does not give direct information about the delivery of oxygen to the tumor cells. The TRITC-dextran bolus follows the plasma current, however, the red blood cells are the component of the blood that transports the oxygen to the tissue [56]. Since red blood cells cannot move faster than plasma in the blood flow [20], BST represents a theoretical minimum time for red blood cell supply. It could happen in thin capillaries that the circulation is mainly conformed of plasma (local hemodilution) [20] and this cannot be detected in the method for calculating the BST. Nevertheless, it has been shown that the red blood cell flux not necessarily reflects the supply of oxygen in tumor tissue due to the fast depletion for oxygen of erythrocytes inside the tumor vasculature [53].

For the calculation of BST, the time of maximum fluorescence intensity in the main supplying artery (MSA) of the tumor was used as the time reference. A proper choice of the pixels or ROI selected for reference in the MSA was important in order to be able to compare the BSTs of different tumors. This is however not an easy task, since it was desirable to select the reference at approximately the same vascular distance from the tumor. Another limitation regarding the selection of the reference in the MSA is that some big tumors had grown over the MSA thereby taking it out of the focus when imaging, or totally impeding them from being observed in the

movies. For this reason some tumors were discarded from the sample included in the BST calculations. Only tumors with visible MSAs were used for quantification of the BST.

Notwithstanding the limitations of the BST calculation method, all the tumors (tumors treated with cyclic hypoxia and control tumors) were imaged in the same way, and under the same conditions. Therefore, the limitations apply equally to all the obtained data and the noise should be comparable for both groups of tumors, and comparable to what has been published before in [52, 51] when applying this same method for other investigations.

5.2 Discussion of the results

5.2.1 Vascular morphology

The morphological images of the tumors (Figures 4.8 and 4.9) give a qualitative impression of the vasculature in the tumors. One difference that was evident from the vascular masks was the higher vessel density in the tumors belonging to the mice treated with cyclic hypoxia. Another feature that was visible from the morphology images was the intratumor heterogeneity. This was specially evident in the control tumors, in which a higher vessel density characterized the peripheral regions in comparison to the central region of the tumors. However, differences in vessel diameter were not obvious from the images.

The vascular masks produced from the morphological images allowed the quantification of the vessel length densities, vascular area fraction, interstitial distance and vessel diameter. From these quantifications, qualitative differences observed between the images of the morphology could be confirmed.

Vessel density

The parameters used for the quantification of the vascular density were the vascular length density, the vascular area fraction and the interstitial distance.

The vascular length density (total vessel length per μm^2) between the two tumor groups (Fig. 4.10) showed a trend towards higher values in the tumors treated with cyclic hypoxia. The vascular area fraction of a tumor (# of pixels within the vascular mask / # of pixels in the whole tumor) was significantly higher for the tumors subjected to cyclic hypoxia than for the control tumors ($p = 0.046$). This

result has important implications supporting higher vessel densities in the treated tumor. Lastly, the interstitial distance in the treated tumors was shorter than in the control groups ($p = 0.034$). This means that the vessels in the tumors exposed to cyclic hypoxia were closer together than the vessels in the control tumors, confirming the evidence of higher vessel density in the treated than in the control tumors. It is of relevance that the interstitial distances in all the studied tumors (treated and control) did not exceed 20 μ m which is under the oxygen diffusion limit threshold (100-200 μm), and therefore it is not probable that the studied tumors had regions of chronic hypoxia or necrosis.

Significantly higher vessel densities in tumors subjected to cyclic hypoxia treatment have previously been observed in intradermal tumors of the same tumor line [6], where the microvascular density was quantified from histological sections of the tumors. The observed increased vessel density in the tumors exposed to cyclic hypoxia is most likely due to enhanced angiogenesis induced by hypoxia. This is expected since, as mentioned before, under hypoxic conditions HIF-1α dimerizes with HIF-1β resulting in transcription of genes that stimulate angiogenesis, such as VEGF-A, which has been shown to be over-expressed in tumors subjected to cyclic hypoxia [6].

Vessel diameter

The mean vessel diameter was calculated averaging all the vessel diameters in the vascular masks. The results of the quantification of this parameter for the tumors treated with cyclic hypoxia and the control tumors are shown in Figure 4.13. As can be observed from the plot, there was no visible trend or difference between the vessel diameters of the treated and control tumors ($p = 0.791$). It is interesting though that the differences in vessel density found between the tumors treated with cyclic hypoxia and the control tumors does not respond to difference in vessel diameter. This means that the increase in vessel density is mainly due to the generation of new vessels with similar diameters and not from large differences in vessel diameters within the tumors.

Intratumor heterogeneity

The observation of the morphology images of the control tumors gave rise to the hypothesis that these tumors presented larger spatial variations in vessel density. Therefore, tumors were divided into 3 concentric regions of interest (ROIs) delimited by lines drawn at $R/3$, $2R/3$ and R, where R was the radius of the tumor, as described previously. However, after plotting the vascular density parameters, it was

observed that the middle ROI (between $R/3$ and $2R/3$) did not vary substantially from the central ROI (circumscribed by a line drawn at $R/3$), and that these central and middle regions did vary greatly from the peripheral ROI. Because of that, it was decided to present the intratumor heterogeneity results with only the two relevant concentric ROIs in the tumors: a central ROI (circumscribed by a line drawn at $2R/3$) and a peripheral ROI (between the lines drawn at $2R/3$ and R). This is shown in Figure 4.14.

The vascular area fraction (VAF) in treated and control tumors for the central ROI and peripheral ROI are shown in Figures 4.15 and 4.16, respectively. The difference in the VAF between the treated and control groups was greater for the central region ($p = 0.032$) than the peripheral region ($p = 0.225$).

The results of this section indicate that the tumors exposed to cyclic hypoxia developed more homogeneous vascular networks than the control tumors. This could be because of increased angiogenesis throughout the tumor, due to upregulation of angiogenic factors. VEGF-A is likely to be responsible of this enhanced angiogenesis, since it was found to be over-expressed in intradermal tumors subjected to the same cyclic hypoxia treatment [6].

5.2.2 BST

As shown in Figure 4.18, it was observed that the tumors exposed to cyclic hypoxia displayed a higher heterogeneity in blood supply times throughout the vascular network than the control tumors represented in Figure 4.19. These heterogeneities in BST in the tumors can be better recognized from the BST histograms (shown in the right panels of Figs. 4.18 and 4.19). A broader BST histogram corresponds to a tumor with larger variations in BST throughout the vascular network, whereas a narrow BST histogram correspond to tumors with little variations in the blood supply. Tumors with little variations in BST can therefore be related a more effective blood supply, indicating that the whole tumor is supplied of blood in short times. Conversely, large variations in BST can be related to heterogeneous blood flow with poor (and perhaps insufficient) blood supply in some regions of the tumor.

The median BST value of each tumor in the treatment and control groups was plotted in Figure 4.20. The median BST value was chosen instead of the mean value because it has been observed from previous experiments that the median is a more robust value, less affected by the noise. In Fig. 4.20 a trend towards higher median BSTs in the treated tumors than in the control tumors is noticeable. However, this

apparent difference was not statistically significant ($p = 0.148$). One possible reason for this is that the samples of the treated and control tumors were smaller (7 treated tumors and 8 control tumors) than in the analysis of the morphology (10 tumors in each group). The reduced number in the samples for the BST analysis was due to some movies that did not pass the quality control to ensure a reliable determination of the BSTs.

Nevertheless, the trend towards higher BST in tumors subjected to cyclic hypoxia could be justified by the fact that hypoxia induced angiogenesis and vascular remodeling result in new vessels that may be immature and contribute to a less efficient supply of blood.

5.2.3 Tumor growth

The transfection of GFP into the tumor cells not only made it possible to monitor a correct implantation of the spheroids, but also facilitated the observations of tumor growth during these experiments. This can be observed in Figures 4.4 and 4.5, where a better contrast between the boundaries of the tumor and the rest of the tissue is evident in the GFP images. For this reason, the area of the tumors at different time points throughout the experiment was calculated by drawing the tumor perimeter on the GFP images. Another feature that can be observed in Figures 4.4 and 4.5 is that no vasculature is visible in the tumors on day 1 and 3. This indicates that the vasculature inside the tumor developed after the third day after implantation of spheroids.

From the area calculations, Figure 4.6 was obtained; in this figure it is shown that the tumors subjected to cyclic hypoxia grew slower than the control tumors. It is interesting that tumors between the two groups had almost identical average sizes on the third day of the experiment. This could mean that the differences in growth rate started once the tumors had developed their vascular networks.

Figure 4.7 shows the area of the tumors in the treated and control groups on the last day of the experiments. Since, as mentioned before, the sizes of the implanted spheroids did not vary significantly between the two groups ($p > 0.05$) and that the size of the tumors in the two groups was equal in average on day 3, the differences in sizes at the end of the experiment respond to different growth rates between the group that underwent cyclic hypoxia and the control group. This difference in area at the end of the experiment was statistically significant ($p = 0.045$). Differences in tumor sizes within tumors exposed to cyclic hypoxia and control tumors have also

been observed in a study by Cairns *et al.* [4]. In this study they showed that tumors exposed to cyclic hypoxia grew significantly slower than control tumors, but that in spite of this, the acute hypoxia treatment enhanced lymph node metastasis.

The reduced growth rate in tumors exposed to cyclic hypoxia occurred in spite of the increased vessel densities in these tumors. However, the trend towards higher BST values in the treated tumors might explain this phenomenon since higher BSTs are related to less efficient supply of blood and, thus, nutrients to the tumor, thereby limiting its growth rate.

Other experiments involving cyclic hypoxia in tumors have reported increased metastases in tumors that underwent cyclic hypoxia compared to control tumors [3, 4, 6, 57]. However, in this experiment it was not possible to study metastatic dissemination since metastasis in this tumor line occurs after certain sizes that cannot be reached when the tumor size is restricted by the window chambers.

5.3 Suggestions for future work

As future work, it would be interesting to perform the same experiments in different tumor lines, perhaps with a lower growth rate or a different angiogenic profile, and compare the results for the different tumor models.

Investigation of the molecular mechanisms that arise as response to cyclic hypoxia is another interesting possible topic. This window chamber method for the study of effects of cyclic hypoxia in tumors could also include a group of mice that received the cyclic hypoxia treatment combined with an antiangiogenic treatment

Since it was observed that the vessel density is increased in tumors exposed to cyclic hypoxia, it would be relevant to investigate if the cyclic hypoxia treatment has consequences for the interstitial fluid pressure of the tumors.

Another important suggestion for future work is to acquire the images with a confocal microscope in order to eliminate the limitations of having three dimensions projected into two, and study the vascular networks as bidimensional slices, or as 3-dimensional structures reconstructed from the slices.

It would also be relevant to investigate the metastatic potential of tumors treated with cyclic hypoxia and if there is a correlation with this and the BST in tumors. This would however require the use of a different tumor line for the experiments.

Chapter 6

Conclusions

Exposure to cyclic hypoxia in A-07-GFP melanoma xenografts resulted in differences in growth rate, morphology and function of the vascular networks in the tumors compared to control tumors. Regarding the differences in the morphology, tumors treated with cyclic hypoxia displayed increased vascular densities and vascular networks with less intratumor heterogeneities. In relation to the function, treated tumors had more heterogeneous BST values in the vasculature and showed a trend towards higher BST median values than the control tumor. The higher vessel density, lower intratumor heterogeneity and higher median BST values in the tumors treated with cyclic hypoxia are likely to occur due to hypoxia-induced angiogenesis which promotes the development of new vessels and remodeling of the vascular networks. These mechanisms can increase the vascular densities in the tumors. Moreover, the presence of many new immature vessels can result in a less efficient circulation in the tumor, and thus, higher BST values. The tumor growth rate was lower in the tumors treated with cyclic hypoxia. This can be related to the inefficient blood (and thus, nutrient) supply reflected in the trend towards high BST values of the treated tumors.

Bibliography

[1] P. Vaupel and A. Mayer. **Hypoxia in cancer: significance and impact on clinical outcome.** *Cancer Metastasis Rev.,* 26: 225-239 (2007).

[2] S.M. Evans and C.J. Koch. **Prognostic significance of tumor oxygenation in humans.** *Cancer Letters,* 195: 1-16 (2003).

[3] R. A. Cairns, T. Kalliomaki and R. P. Hill. **Acute (cyclic) hypoxia enhances spontaneous metastasis of KHT murine tumors.** *Cancer Res.,* 61: 8903-8908 (2001).

[4] R. A. Cairns and R. P. Hill. **Acute hypoxia enhances spontaneous lymph node metastasis in an orthotopic murine model of human cervical carcinoma.** *Cancer Res.,* 64: 2054-2061 (2004).

[5] E. K. Rofstad, K. Galappathi and B. Mathiesen. **Fluctuating and diffusion-limited hypoxia in hypoxia-induced metastasis.** *Clin. Cancer Res.,* 13: 1971-1978 (2007).

[6] E. K. Rofstad, J-V. Gaustad, T. A. M. Egeland, B. Mathiesen and K. Galappathi. **Tumors exposed to acute cyclic hypoxic stress show enhanced angiogenesis, perfusion and metastatic dissemination.** *Int. J. Cancer,* 127: 1535-1546 (2010).

[7] D. G. Hirst and J. Denekamp. **Tumour cell proliferation in relation to the vasculature.** *Cell Tissue Kinet.,* 12: 31-42 (1979).

[8] Ian F. Tannock. **Tumor physiology and drug resistance.** *Cancer and Metastasis Reviews,* 20: 123-132 (2001).

[9] R. K. Jain. **Tumor angiogenesis and accessibility: Role of vascular endothelial growth factor.** *Seminars in Oncology,* 29: 6, suppl. 16: 3-9 (2002).

[10] J. M. Brown and A. J. Giaccia. **The unique physiology of solid tumors: opportunities (and problems) for cancer therapy.** *Cancer Res.,* 58: 1408 - 1416 (1998).

[11] P. Carmeliet and R. K. Jain. **Angiogenesis in cancer and other diseases.** *Nature,* 407: 249 -257 (2000).

[12] J. Folkman and Y. Shing. **Angiogenesis.** *The Journal of Biological Chemistry,* 267, 16: 10931 - 10934 (1992).

[13] D. W. Siemann. **Vascular targeting agents. Horizons in Cancer Therapeutics: From Bench to Bedside.** *Meniscus Limited,* 3(2): 4-15 (2002).

[14] G. Bergers and L. E. Benjamin. **Tumorigenesis and the angiogenic switch.** *Nature Reviews,* 3: 401 - 410 (2003).

[15] D. Hanahan and J. Folkman. **Patterns and emerging mechanisms of the angiogenic switch during tumorigenesis.** *Cell,* 86: 353 - 364 (1996).

[16] B. R. Zetter. **Angiogenesis and tumor metastasis.** *Annu. Rev. Med.,* 49: 407- 424 (1998).

[17] R. K. Jain, K. Schlenger, M. Höckel and F. Yuan. **Quantitative angiogenesis assays: Progress and problems.** *Nature medicine,* 3.11: 1203 -1208 (1997).

[18] W. Risau. **Mechanisms of angiogenesis.** *Nature,* 386: 671 - 674 (1997).

[19] P. Vaupel, F. Kallinowski and P. Okunieff. **Blood flow, oxygen and nutrient supply, and metabolic microenvironment of human tumors: A review.** *Cancer Research,* 49: 6449-6465 (1989).

[20] R. K. Jain. **Determinants of tumor blood flow: a review.** *Cancer Research,* 48: 2641-2658 (1988).

[21] E. M. Sevick and R. K. Jain. **Geometric resistance to blood flow in solid tumors perfused ex vivo: effects of tumor size and perfusion pressure.** *Cancer Research,* 49: 3506-3512 (1989).

[22] M. W. Dewhirst, R. Richardson, I. Cardenas-Navia and Y. Cao. **The relationship between tumor physiologic microenvironment and angiogenesis.** *Hematol. Oncol. Clin. N. Am.,* 18: 973-990 (2004).

[23] M. F. Adam, E. C. Gabalski, D. A. Bloch, J. W. Oehlert, J. M. Brown, A. A. Elsaid, H. A. Pinto and D. J. Terris. **Tissue oxygen distribution in head and neck cancer patients.** *Head & Neck,* 21, 2:146-153 (1999).

[24] P. Vaupel. **The role of hypoxia-induced factors in tumor progression.** *Ongologist,* 9: 10-17 (2004).

[25] K. G. Brurberg, B. A. Graff and E. K. Rofstad. **Temporal heterogeneity in oxygen tension in human melanoma xanografts.** *British Journal of Cancer,* 89: 350-356 (2003).

[26] M. W. Dewhirst. **Relationships between cycling hypoxia, HIF-1, angiogenesis and oxidative stress.** *Radiation Research,* 172: 653-665 (2009).

[27] P. Vaupel and A. Mayer. **Hypoxia in cancer: significance and impact on clinical outcome.** *Cancer Metastasis Rev.,* 26: 225-239 (2007).

[28] R.H. Thomlinson and L.H. Gray. **The histological structure of some human lung cancer and the possible implications for radiotherapy.** *Br. J. Cancer,* 9: 539-549 (1955).

[29] E. J. Hall and A. J. Giaccia. **Radiobiology for the radiologist.** *Lippincott Williams & Wilkins,* USA, 2006.

[30] J. M. Brown. **The Hypoxic Cell : A Target for Selective Cancer Therapy.** *Cancer Res.,* ;59: 5863-587 (1999).

[31] K. G. Brurberg, J. V. Gaustad, C. S. Mollat and E. K. Rofstad. **Temporal heterogeneity in blood supply in human tumor xenografts.** *Neoplasia,* 10: 727-735 (2008).

[32] M. W. Dewhirst. **Concepts of oxygen transport at the microcirculatory level.** *Semin. Radiat. Oncol.,* 8: 143-150 (1998).

[33] D. J. Chaplin, R. E. Durand and P. L. Olive. **Acute hypoxia in tumors: implications for modifiers of radiation effects.** *Int. J. Radiation Oncology Biol. Phys.,* 12: 1279-1282 (1986).

[34] M. J. Trotter, D. J. Chaplin, R. E. Durand and P. L. Olive. **The use of fluorescent probes to identify regions of transient perfusion in murine tumors.** *Int. J. Radiat. Oncol. Bio. Phys.,* 16: 931-934 (1989).

[35] R. M. Sutherland. **Tumor hypoxia and gene expression: implications for malignant progression and therapy.** *Acta Oncologica,* 37: 567-574 (1998).

[36] P. Carmeliet, Y. Dor, J. M. Herbert, D. Fukumura, K. Brusselmans, M. Dewerchin, M. Neeman, F. Bono, R. Abramovitch, P. Maxwell, C. J. Koch, P. Ratcliffe, L. Moons, R. K. Jain, D. Collen and E. Keshert. **Role of HIF-1α in hypoxia mediated apoptosis, cell proliferation and tumour angiogenesis.** *Nature,* 394: 485-490 (1998).

[37] C. W. Pugh and P. Ratcliffe. **Regulation of angiogenesis by hypoxia: role of the HIF system.** *Nature Medicine,* 9: 677-684 (2003).

[38] P. Martinive, F. Defresne, E. Quaghebeur, G. Daneau, N. Crokart, V. Grégoire, B. Gallez, C. Dessy and O. Feron. **Impact of cyclic hypoxia on HIF-1α regulation in endothelial cells - new insights for anti-tumor treatments.** *FEBS Journal,* 276: 509-518 (2009).

[39] D. Hanahan, G. Christofori, P. Naik and J. Arbeit. **Transgenic mouse models of tumor angiogenesis: the angiogenic switch, its molecular controls, and prospect for therapeutic models.** *Eur. J. Cancer,* 32: 2386-2393 (1996).

[40] L. H. Gray, A. D. Conger, M. Ebert, S. Hornsey and O. C. Scott. **The concentration of oxygen dissolved in tissues at the time of irradiation as a factor in radiotherapy.** *Br. J. Radiol.* 26: 628-648 (1953).

[41] M. Höckel, K. Schlenger, B. Aral, M. Milze, U. Schäffer, and . Vaupel. **Association between tumor hypoxia and malignant progression in advanced cancer of the uterine cervix.** *Cancer Research,* 56:4509-4515 (1996).

[42] River Laboratories International, Inc. 2011. Available:
http://www.criver.com/en-US/ProdServ/ByType/ResModOver/ResMod/Pages/NuNuNudeMouse.aspx
Last accessed 22nd May 2011.

[43] Taconic Farms, Inc. 2006-2011. Available:
http://www.taconic.com/wmspage.cfm?parm1=769
Last accessed 22nd May 2011.

[44] E. K. Rofstad. **Orthotopic human melanoma xenograft model systems for studies of tumour angiogenesis, pathophysiology, treatment sensitivity and metastatic pattern.** *Br. J. Cancer,* 70(5): 804Ð812 (1994).

[45] A. J. W. G. Visser and O. J. Rolinski. **Basic photophysics.** *American Society for Photobiology.* (2010) Available:
http://www.photobiology.info/Visser-Rolinski.html
Last accessed 29th May 2011.

[46] R. K. Jain, L. L. Munn and D. Fukumura. **Dissecting tumour pathophysiology using intravital microscopy.** *Nat. Rev. Cancer,* 2: 266-276 (2002).

[47] P. N. Prasad. **Introduction to biophotonics.** *John Wiley & Sons, Inc.,* USA (2003).

[48] C. de Lange Davies and B. Stokke. **Biophysical nanotechnologies: Lecture notes TFY 4265 Biophysical Microtechniques.** *Biophysics and Medical Technology, Dept. of Physics, NTNU;* Norway (2008).

[49] E. K. Rofstad, A. Wahl, C. de L. Davies and T. Brustad. **Growth characteristics of human melanoma multicellular spheroids in liquid-overlay culture: comparisons with the parent tumor xenografts.** *Cell Tissue Kinet.,* 19: 205-216 (1986).

[50] E. M. Huuse. **Vitalmikroskopistudier av humane melanoma-xenografter.** *Master Thesis, Institute of Physics, NTNU and Department of Radiation Biology, Institute for Cancer Research,* The Norwegian Radium Hospital, Norway, 2006.

[51] K. S. Øye, G. Gulati, B. A. Graff, J. V. Gaustad, K. G. Brurberg and E. K. Rofstad. **A novel method for mapping the heterogeneity in blood supply to normal and malignant tissues in the mouse dorsal window chamber.** *Microvascular Research,* 75: 179-187 (2008).

[52] J.-V. Gaustad, K. G. Brurberg, T. G. Simonsen, C. S. Mollatt and E. K. Rofstad. **Tumor vascularity assessed by magnetic resonance imaging and intravital microscopy imaging.** *Neoplasia,* 10: 354-362 (2008).

[53] M. W. Dewhirst, E. T. Ong, B. Klitzman, T. W. Secomb, R. Z. Vinuya, R. Dodge, D. Brizel and J. F. Gross. **Perivascular oxygen tensions in transplantable mammary tumor growing in dorsal flap window chamber.** *Radiat. Res.,* 130: 171-182 (1992).

[54] M. W. Dewhirst. **Concepts of oxygen transport at the microcirculatory level.** *Semin. Radiat. Oncol.,* 8: 143-150 (1998).

[55] P. Martinive, F. Defresne, C. Bouzin, J. Saliez, F. Lair, V. Grégoire, C. Michiels, C. Dessy and O. Feron. **Preconditioning of tumor vasculature and tumor cancer cells by intermittent hypoxia: implications for anticancer therapies.** *Cancer Res.,* 66: 11736-11744 (2006).

[56] P. Vaupel. **Oxygenation of human tumors.** *Strahlenther. Onkol.,* 166: 377-386 (1990).

[57] E. K. Rofstad, J. V. Gaustad, T. A. M. Egeland, B. Mathiesen and K. Galappathi. **Tumors exposed to cyclic hypoxic stress show enhanced angiogenesis, perfusion and metastatic dissemination.** *International Journal of Cancer,* 127: 1535 - 1546 (2010).